Journal of Marine Research, 72, 127–163, 2014

Anatomy of a Langmuir supercell event

by A. E. Gargett[1,2], D. K. Savidge[3], and J. R. Wells[4]

ABSTRACT

Langmuir supercells (LS), which are Langmuir circulations (LC) extending over full water column depth during storms and revealed by high water column backscatter from surface-origin microbubbles and bottom-origin sediment, were discovered in 2003 during several months of measurements in 15 m of water near the coast of New Jersey. Both the structures themselves and the specific forcing conditions under which they occur have been documented elsewhere. This paper provides an account of the broader oceanographic setting of supercell events, focusing on conditions at the start and end. The start of events is associated with the presence of surface waves of intermediate type that "feel bottom" with amplitudes sufficiently large to resuspend sediment and achievement of three conditions for full-depth LC: an unstratified water column, $La < \sim 0.3$ and $|Ra| < 10^5$, where Ra and La are dimensionless parameters derived from scaling of the wave-averaged momentum equation. Event cessation is associated with failure of one of the latter two conditions or the reappearance of stratification. There is no fixed order in which conditions necessary for full-depth LC are met or fail.

Comparison with data from a deeper site off Georgia suggests that coherent full-depth Langmuir circulations will not generally be observed in unstratified water columns much deeper than 25–30 m, a depth determined primarily by the wavelength of surface waves generated by typical storms.

We also document two features of LC acting in the surface layer of the stratified water column that existed prior to onset of the prototype LS event. First, LC confined to the surface layer generated first mode internal waves with frequency that of the stratified interior. Secondly, active surface layer LC did not act efficiently as direct agents of mixed layer deepening, which occurred primarily in two separate episodes of Richardson number lowered by increased shear. Instead, as a result of quasi-organized structure and enhanced vertical penetration relative to stress-driven turbulence, the primary role of LC may be to increase efficiency of momentum transfer to the surface layer, enhancing surface layer acceleration and contributing to onset of the shear instability that does deepen the surface layer.

1. Introduction

In April 2003, a Vertical Beam Acoustic Doppler Current Profiler (VADCP) was installed at the B node (39°27.69′N, 74°14.68′W, 15 m mean water depth) of LEO15, a cabled observatory that then existed approximately 6 km off the coast of New Jersey. Within

1. Institute of Ocean Sciences, Sidney, B.C., Canada, and Old Dominion University, Norfolk, VA.
2. Corresponding author ***e-mail: gargettann@gmail.com***
3. Skidaway Institute of Oceanography, Savannah, GA.
4. University of Hawaii, Honolulu, HI.

a month, observations revealed a striking event in which the entire water column filled with high backscatter during one of the "nor'easters" that are the typical synoptic scale storms in the region. Detailed examination showed that backscatter was highly patterned and the pattern was strongly correlated with fluctuation vertical velocity w', measured directly by the vertical beam of the VADCP. High surface-origin backscatter plumes were associated with downward w', high bottom-origin backscatter plumes with upward w'. The full three-dimensional velocity field available from the VADCP measurements during this event was demonstrated to be compatible with that of full-depth Langmuir circulations (LC) by Gargett et al. (2004), who called the structures "Langmuir supercells" (LS[5]) in tribute to their profound effects on the vertical distribution and horizontal transport of resuspended sediment and accompanying bioactive material on shallow shelves.

The observed characteristics of supercells are thoroughly explored in Gargett and Wells (2007), who find that as long as wind/wave forcing remains approximately constant, LS have stable crosswind horizontal scale $L \sim (4-6)H$, where L is horizontal distance between successive surface convergences and H is water column depth. This structural stability contrasts sharply with the deepwater case in which structures with initially well-defined crosswind scale quickly break down into more disorganized "Langmuir turbulence" (McWilliams et al., 1997) but is consistent with the stability analysis of Rosenhead (1929; see also Thorpe, 1992), who finds stability of paired vortices in a finite depth channel provided $H/(L/2) < 0.709$, or $L/H > \sim 3$. The LS observations of Gargett and Wells (2007) have been compared with steady-state results obtained with shallow-water Large Eddy Simulations (LES; Tejada-Martínez and Grosch, 2007) that include vortex force of Craik and Liebovich (1976), hereafter the C-L vortex force, that parameterizes forcing associated with surface wave Stokes drift. All observationally available characteristics agree well with those resulting from LES driven by wind/wave forcing comparable to that of the observations.

In separate examination of a broader subset of the 6-month data set obtained at LEO15, Gargett and Grosch (2014) delineated the range of wind/wave/buoyancy forcing necessary for LS in an unstratified water column. A new scaling of the momentum equation for cases of mixed forcing (simultaneous presence of wind stress forcing, C-L vortex forcing and destabilizing surface buoyancy flux) produced two parameters that proved successful in identifying cases where a single forcing process dominates turbulence production. The first parameter, a Langmuir number,

$$La \equiv \left(\frac{u_*}{u_{S0}} \right), \tag{1}$$

is the ratio of surface stress velocity u_* to surface spectral Stokes velocity u_{S0} (defined by Gargett and Grosch [2014] as an integral over wavenumber; see their Appendix]. $La >> 1$

5. The term "Langmuir supercells" has until now been abbreviated as LSC; however, with the advent of "Lagrangian coherent structures" (LCS) in oceanographic data analysis, it seems prudent to avoid possible confusion by replacing LSC with LS.

implies C-L vortex forces negligible relative to inertial (nonlinear) forces associated with stress driving, just as the more familiar Reynolds number $Re >> 1$ implies viscous forces negligible relative to inertial forces. The second parameter, a generalized Rayleigh number,

$$Ra \equiv \left(\frac{\alpha_T g}{k_T}\right) Q t_*^2 = \left(\frac{\alpha_T g}{k_T}\right) \frac{Q}{g_*^2}, \tag{2}$$

where t_* is a characteristic time scale, $g_* = t_*^{-1}$ the associated characteristic growth rate, g is acceleration of gravity, k_T is the thermal conductivity and α_T is the thermal expansion coefficient of seawater, describes the importance of surface heat flux: $Q > 0$ is destabilizing to the ocean. The scaling of Gargett and Grosch (2014) uses a characteristic time scale for LC growth derived by Leibovich (1977):

$$t_* \equiv \left(\frac{dU_S}{dx_3}\frac{dU}{dx_3}\right)^{-1/2}, \tag{3}$$

the inverse geometric mean of mean shear $dU/dx_3 \sim u_*/H$ and Stokes shear dU_S/dx_3 evaluated at depth $x_3 = -0.2H$ (shear at fixed depth fraction is a more appropriate measure of effect on the whole water column than is shear at fixed depth; Harcourt and D'Asaro, 2008; Gnanadesikan, 1996). Use of this time scale (in place of the geometric mean of viscous and thermal diffusion time scales that appears in the classical Rayleigh number) assumes that LC are always present, though not necessarily dominant, in the wind/wave/buoyancy-forced surface layer. Gargett and Grosch (2014) observed LS only when $La < 10^{-0.5} \sim 0.3$ and $0 < Ra < 10^5$.

With original concentration on steady-state LS structures, and subsequently on the forcing conditions associated with them, there has been as yet no overall description of a LS event, defined here as the presence of organized full-depth LC revealed by vertically overlapping backscatter features originating from surface and bottom. While full-depth LC without associated bottom backscatter signatures are possible, for example, if the sea bottom were rock or gravel, the silt/sand sediments characteristic of the observational sites discussed here produce bottom-origin signatures when LC reach full depth. The coincidence of full-depth LC and bottom-origin sediment clouds requires that, at the time LC reach the bottom, resuspended sediment is available for entrainment; we will demonstrate that this requirement is fulfilled. The present paper provides details of evolution of the prototype event that led Gargett et al. (2004) to the original identification of LS. Although primarily descriptive, the paper also addresses the question "how deep?"; that is, how deep does an unstratified water column have to be before supercell events no longer occur?

Data and processing are described in Section 2, while temporal variation in forcing fields, event-scale ocean response, and turbulent structures during the prototype LS event are presented in Section 3. Section 4 lays out requirements for full-depth LC, then demonstrates the availability of resuspended sediment when the LC reach bottom. Section 5 compares the prototype with two additional events, verifying features common to event onset and

cessation. Section 6 uses the results of this analysis and observations from a deeper site to address the question "how deep?" Section 7 summarizes conclusions, suggests areas of needed research focus, and emphasizes the importance of LS events for sediment transport on shallow shelves.

2. Data and processing

Atmospheric data necessary to quantify forcing of surface-layer turbulence at LEO15 were taken at a meteorological tower then located on the beach shore ~6 km west of the node. Backed by an extensive marsh, the tower had excellent exposure: tower wind speed and direction are highly correlated with those measured at a nearby offshore buoy (Münchow and Chant, 2000). Before computing derived quantities such as wind stress τ or surface buoyancy flux B_o, tower variables were averaged over 4 min for consistency with sampling of sea surface and bottom temperatures at Node B. In the absence of rainfall observations, no corrections were made for possible freshwater effects on surface buoyancy flux. Estimates suggest that the additional term is usually small, hence it is assumed that $B_o = \frac{g}{\rho_o C_p T_o} Q$, where Q is heat flux, and ρ_o, T_o, and C_p are representative density, temperature and specific heat at constant pressure of seawater. A bottom-tethered CTD (Conductivity-Temperature-Depth [pressure] recorder) at the node provided sporadic temperature (T) and salinity (S) profiles. Profiling was suspended during storms because of the danger of tangling the tether in high seas.

Water velocities $[u, v, w]$ in instrument coordinates were derived from VADCP measurements with vertical resolution of 0.4 m, starting 1 m above bottom. Data were continuosly sampled at 1s and returned as sequential records of length ~2.4 hr, a period short enough that forcing conditions and water depth could be considered approximately constant but long enough to contain multiple LS when they occurred. Continuous recording was broken into sessions of 4–5 days because, for unknown reasons, instrument-identified errors increased rapidly with time thereafter. While each record has a unique identifier ("sss.nnn," where nnn is sequential record number within session number sss), here for brevity we will refer simply to consecutive record number within three time periods[6], one each in May, September and October, that include the LS events considered. On event timescales, both forcing fields and in-water fields are averaged over record lengths; because absolute time is unimportant, time series are presented as functions of record number within each event.

Sampling frequency of 1 Hz resolved dominant velocities of surface gravity waves that appear at the node with frequencies higher than those of turbulent eddies advected past by weak tidal currents; thus wave velocities could be removed by low-pass filtering in the time domain. This process requires time-continuous data and hence could only be

6. For possible cross-reference with other papers, the May period consists of Records 043.000–043.051 (1344UT May 14 to 1425UT May 19, 2003), the September period of Records 128.009–128.025 and (consecutive) 129.000–129.014 (0457UT September 11 to 0046UT September 14, 2003), and the October period of Records 153.024–153.034 and (consecutive) 154.000–154.034 (2003UT October 11 to 0046UT October 14, 2003).

accomplished at height above bottom $h < H_{\min}$, the minimum value of instantaneous surface height (measured in vertical beam backscatter) over the period involved. After filtering, the 1s data were resampled to produce a time series with 10s sample period. Horizontal velocities were calculated assuming first-order homogeneity over beam spread (Gargett and Wells, 2007). Under a frozen field hypothesis, the response function analysis of Gargett et al. (2009) shows that horizontal scales associated with LS are large enough that beam separation effects do not significantly affect first-order estimates of horizontal velocity variances for retained scales. Vertical velocity was measured directly by the VADCP vertical beam, accurately adjusted to vertical by divers. Additional details of VADCP observations at LEO15 and their processing are found in Gargett and Wells (2007) and Gargett et al. (2008, 2009).

Velocities $[u_1, u_2, u_3]$ in the wind coordinates natural to LC (x_1 in the downwind direction, x_2 in the crosswind direction to the left of x_1, and x_3 positive vertically upward from the mean surface) are calculated from instrument-coordinate velocities using observed wind direction. "Mean" flow $[U_1, U_2, U_3 = 0]$ defined as a time average over record length contains slow variation due to tides; thus fluctuation (turbulent) fields $[u_1', u_2', u_3' = w']$ are calculated by removing linear least squares fits over record length from each bin.

A fundamental metric used to gauge turbulence strength is $\overline{< w'^2 >}$, the column-average (overbar) of $< w'^2 >$, vertical velocity variance corrected for noise bias (Gargett et al., 2008) and time-averaged over record length (angle brackets). The column average is taken from the first measurement bin through the bin just below $H_{\min}$, a level that varies with sea state. Significant wave height Hs, surface spectral Stokes velocity u_{s0} and Stokes shears are determined from the VADCP measurement of w' (see Gargett and Grosch, 2014).

3. Time evolution of a LS event

a. Forcing fields and stratification

For the prototype event, the top two panels of Figure 1 show color-coded images of backscatter amplitude A (corrected for range and radial spreading but not calibrated) and fluctuation vertical velocity w' from the vertical beam of the VADCP over a period of ~5 days in May that included a strong nor'easter. Vertical lines in Figure 1 mark records associated with significant features in the development of the LS event that will be discussed in detail below. For the purposes of this paper, we define the "start" of a LS event as occurring when backscatter clouds originating from surface and bottom consistently overlap in depth; the event "ends" when this condition ceases. By this definition, the event in Figure 1 starts in Record 20 and ends in Record 35.

Lettered carets in Figure 1b mark times of the CTD profiles seen in Figure 2 relative to record-averaged values of (c) vector winds, (d) wind stress, (e) significant wave height, (f) surface heat flux and (g) top-to-bottom temperature difference.

Following a period of weak and variable winds, winds from the NE begin to pick up around Record 13, reaching a maximum corresponding to wind stress of ~0.1 N/m^2 in

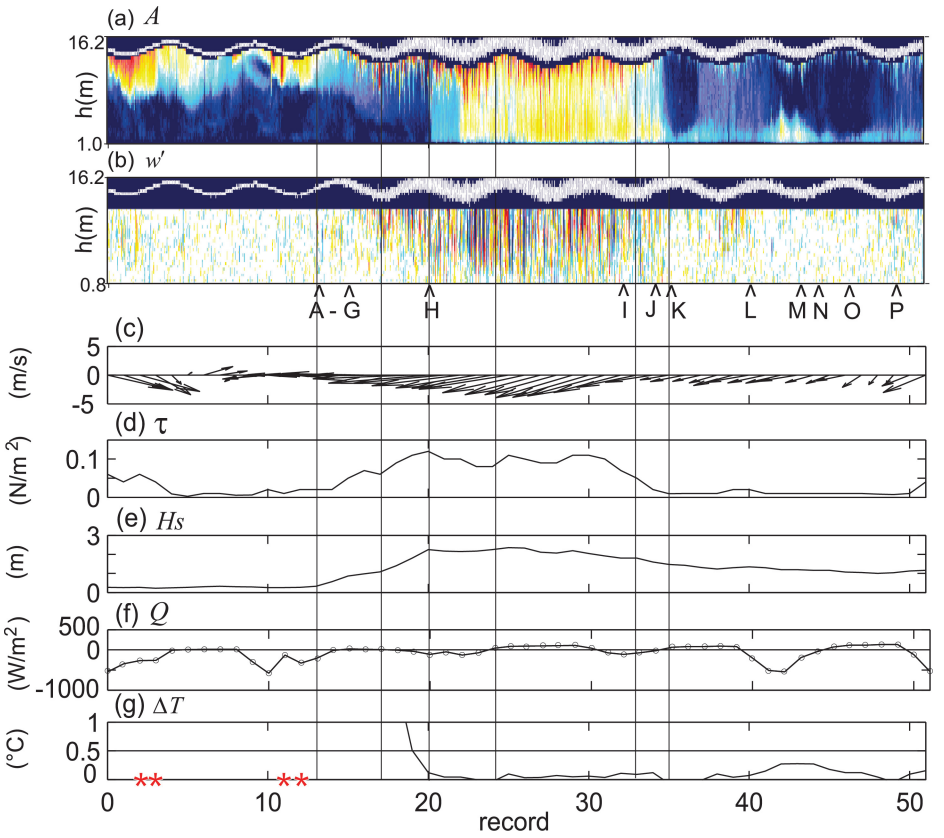

Figure 1. (a) Backscatter amplitude A (corrected for range and radial spreading but not calibrated) and (b) vertical velocity w' ($\pm$ 0.04 m s^{-1}) from the vertical beam of a VADCP deployed on the bottom at the LEO15 observatory off New Jersey. Data start 1344UT May 14 (YD133) and end 1425UT May 19 (YD138), 2003, a period that included a strong "nor'easter," the typical synoptic scale storm in this region. The white line in both panels is surface elevation, showing mean depth of 15 m, semidiurnal tidal variation and increased surface wave heights during the storm. Records are equal lengths of approximately 2.4 h. Record-averaged (c) vector winds, (d) wind stress, (e) significant wave height, (f) surface heat flux, (g) surface to bottom temperature difference. Red stars on the x-axis flag records with indeterminate Stokes velocity.

Record 20. This stress is sustained through Record 30 then declines to pre-storm levels by Record 35. *Hs* increases in step with wind stress but decreases much more slowly than wind stress; *Hs* is still larger at the end of the period than it is before the event began. Before and after the wind event, surface heat flux Q has a diurnal cycle; this cycle is much reduced in magnitude during the LS event, presumably because of cloudy conditions reducing both daytime solar insolation and nighttime back radiation.

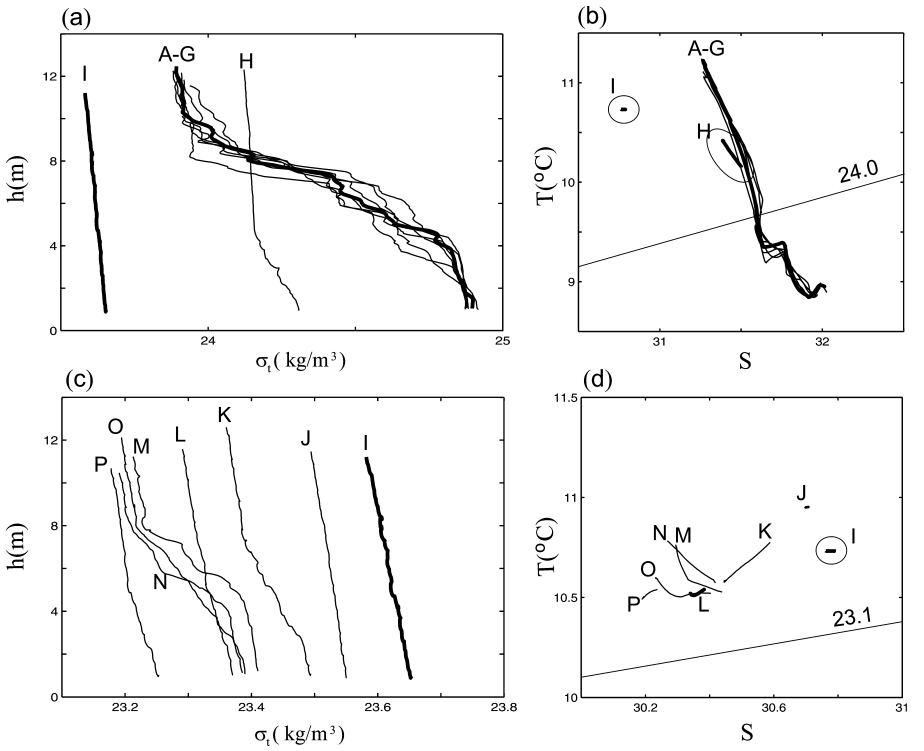

Figure 2. (a) Density profiles before and during the supercell event and (b) associated T/S profiles. The cloud of profiles A–G were taken during Records 13 and 14, as winds increased to storm levels; C (highlighted) was taken in the middle of Record 13. H is a single profile taken at the beginning of Record 20. Furthest left (I) is the first profile obtained after the storm. (c) and (d): Similar plots for profiles taken after the event; note scale changes from (a) and (b).

The top-to-bottom temperature difference ΔT begins at values in excess of 1° but drops to near zero in Record 20. At the start of the wind event (CTD profiles A–G taken during Records 13–15; Fig. 2a), water column stratification is approximately three-layer and determined largely by temperature (Fig. 2b). A relatively well-mixed warm, fresh surface layer is separated from relatively well-mixed colder, saltier bottom water by a region of nearly linear gradient characterized by buoyancy period $T_N \sim 2.5$ min. By CTD H, taken at the beginning of Record 20, the surface layer has deepened dramatically, although slightly stratified water still exists below $h \sim 4$ m. Stratification is assumed to vanish sometime within Record 20, as $\Delta T \rightarrow 0$ and bottom-origin backscatter clouds first appear, although increasing sea state puts an end to profiling until the end of the event, when CTD I reveals that the entire water column has been nearly homogenized.

It is of interest to identify the process responsible for deepening the surface layer. As suggested above and seen in the backscatter record of Figure 1a, surface layer deepening occurs

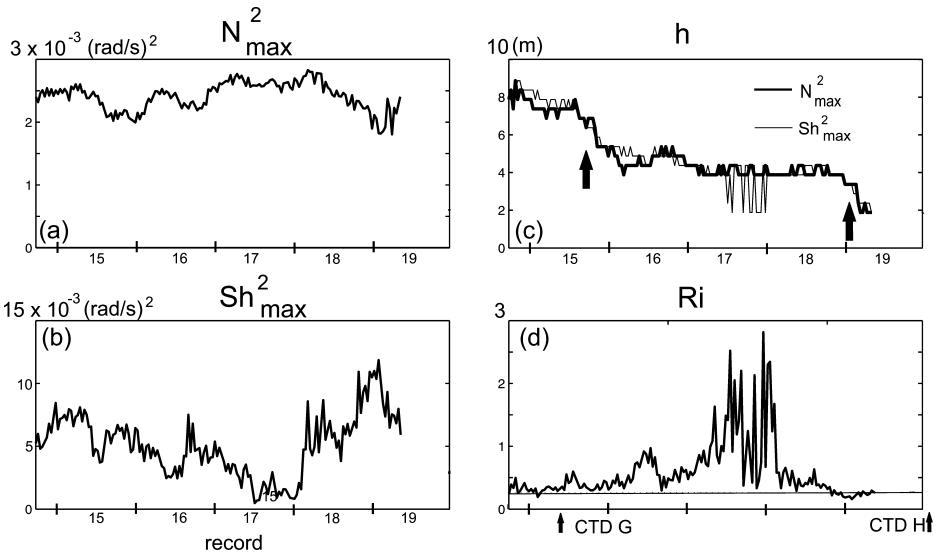

Figure 3. Time series of maximum values of (a) squared buoyancy frequency and (b) squared shear over the period of surface layer deepening after storm onset. (c) The two maxima are essentially coincident in height above bottom until $h = 2$ m, when the estimate of N^2 becomes indeterminate as a result of finite length of the thermistor chain. Arrows indicate periods of surface layer deepening. (d) Richardson number $Ri \equiv N^2_{\max}/Sh^2_{\max}$ characteristic of stability of the surface mixed layer base; the solid horizontal line is $Ri = 0.25$. Fields of w' and A associated with this time period can be identified by the locations shown in Figure 1 for CTDs G (in Record 15) and H (at beginning of Record 20).

in two distinct steps, the first during Records 15–16, the next in Record 20. Two potential deepening processes are LC eroding the top of the stratified interior and shear instability at the surface layer base. For the period when deepening occurs, Figure 3 shows time histories of water column maxima of (a) squared buoyancy frequency $N^2 = (g\rho_o^{-1} d\rho/dz)$ and (b) mean square vertical shear $Sh^2 = (U_z^2 + V_z^2)$ calculated from VADCP measurements of record-mean horizontal velocity. N^2 is an approximation, transforming temperature from continuous thermistor chain measurements to density using the stable T/S relationship observed before the storm (Fig. 2b). Because the thermistor chain is suspended beneath a surface buoy, temperature measurements are restricted to >2 m, the height of the bottom thermistor at high tides. Until that bound is met near the end of the time period shown in Figure 3, the heights at which maxima of N^2 and Sh^2 occur are essentially coincident (Fig. 3c), hence their ratio $Ri \equiv N^2_{\max}/Sh^2_{\max}$ is a meaningful Richardson number for describing stability of the surface layer base. Figure 3c clearly shows the surface layer deepening during two periods (arrows) when Ri is small, although the exact degree of proximity to the value of 0.25 usually taken as a shear instability threshold is uncertain because of the assumption of constant T/S relationship involved in derivation of N^2. Between these periods

lie several hours of high Ri (due primarily to low shear) and effectively constant surface layer depth, despite evidence (Fig. 1ab, see also Fig. 7b) of LC active within the surface layer. Entrainment by LC is demonstrably not an efficient means of deepening the surface layer in the present case; deepening instead occurs predominantly through shear instability. LC do have a basal scouring effect (possibly associated with Hölmböe instability; Strang and Fernando, 2001), clearly revealed here by the entrainment of resuspended sediment once the cells near bottom. However, the effect of this process on surface layer buoyancy, hence mixed layer deepening, is demonstrably of secondary importance in the present case.

Returning to Figure 2c, CTD profiles taken after the event end are a confused jumble of fairly well-mixed (J, L, P) and three-layer structure (K, M, N, O), suggesting lateral interleaving of multiple water masses with relatively small (note scale changes) density contrasts. Post-event mean salinity is lower than any value found in the water column before the event, consistent with water moved from further north on the shelf by the strong downwind transport that is characteristic of LS events (Gargett and Wells, 2007; Tejada-Martínez and Grosch, 2007).

b. Descriptors of turbulence and surface waves

Beneath the same reference images of A and w', Figure 4 presents time series of various derived quantities that are important descriptors of the LS event resulting from the forcings of Figure 1. The characteristic LC growth rate $g_* \equiv t_*^{-1}$ (Fig. 4c) is very low until Record 13, increases steadily until Record 20, then remains relatively constant during the period between Records 20 and 30, when τ and Hs are also approximately constant (Fig. 1). As wind stress drops after Record 30, g_* decreases, first slowly, then rapidly between Records 33 and 35. After the event has ended in Record 35, g_* remains relatively constant through the end of the period, at a level considerably in excess of that before the event.

In Record 13, a dominant wave steepness parameter ε_B (Fig. 4d) abruptly exceeds a breaking threshold of 0.05 proposed by Banner et al. (2000) ($\varepsilon_B \equiv H_p k_p/2$, where k_p is the wavenumber of the peak of the wave displacement spectrum and $H_p = 4\left\{\int_{0.7f_p}^{1.3f_p} F(f)df\right\}^{1/2}$ is a significant wave height of "dominant" waves, those within 30% of the peak), coincident with appearance of the surface-origin backscatter signals typical of LC. Breaking produces quasi-symmetric localized perturbations of the surface velocity field (Leibovich, 1983; Csanady, 1994), resulting in preferential generation of paired vertical vorticity. One might hypothesize that such prestructured vorticity, rotated to horizontal by Stokes drift shear, would be more efficient at generating LC than the randomly oriented vorticity associated with a stress-driven boundary layer, hence that the increase in characteristic LC growth rate g_* is caused by the onset of breaking. However, the observed association does not prove a causal relationship, since onset of breaking may merely reveal pre-existing LC by supplying previously absent microbubble tracers. Further information on this question will be provided by examination of additional LS events (Section 5). In the

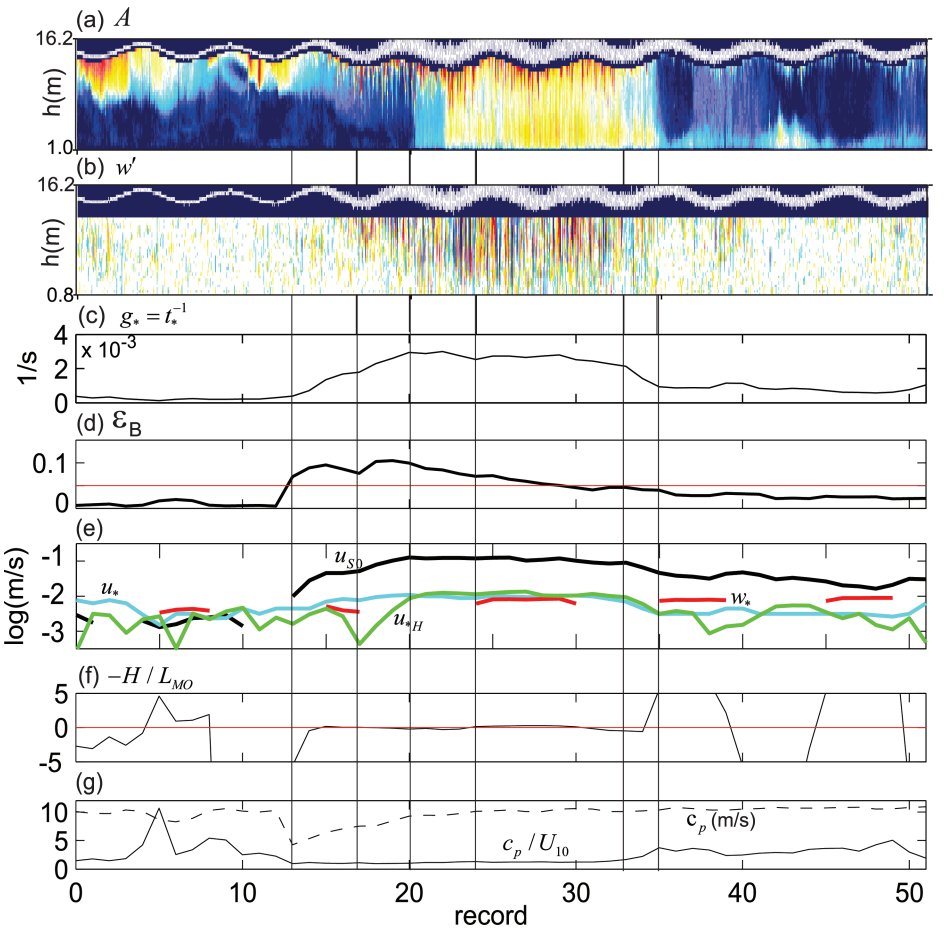

Figure 4. The top two panels are the same fields of (a) A and (b) w' shown in Figure 1, to facilitate intercomparison. (c) LC characteristic growth rate g_*. (d) ε_B, the dominant surface wave breaking criterion of Banner et al. (2000). The red line at 0.05 is a suggested threshold level for breaking. (e) Turbulence scale velocities: surface spectral Stokes velocity u_{S0}, surface stress velocity u_*, bottom stress velocity u_{*H}, and convective scale velocity w_* (for definitions, see text). (f) (Negative) ratio of water depth to Monin-Obukov length scale L_{MO}. (g) Phase speed c_p and wave "age" c_p/U_{10} for the peak of the surface wave displacement spectrum. Vertical lines mark records (13, 17, 20, 24, 33 and 35) shown in more detail in Figure 7.

present event, the breaking criterion is marginally fulfilled until after Record 35, when ε_B falls well below 0.05.

Figure 4e illustrates time evolution of various possible scale velocities for turbulence: surface spectral Stokes velocity u_{S0}, surface stress velocity $u_* = (\tau/\rho_o)^{1/2}$, bottom stress velocity $u_{*H} = (\tau_{*H}/\rho_o)^{1/2}$ (using bottom stress τ_{*H} calculated with the quadratic relationship $\tau_{*H} = \rho_o(2.5 \times 10^{-3})U_{1m}^2$ (Sternberg, 1968; Sherwood et al., 2006), where $U_{1m} =$

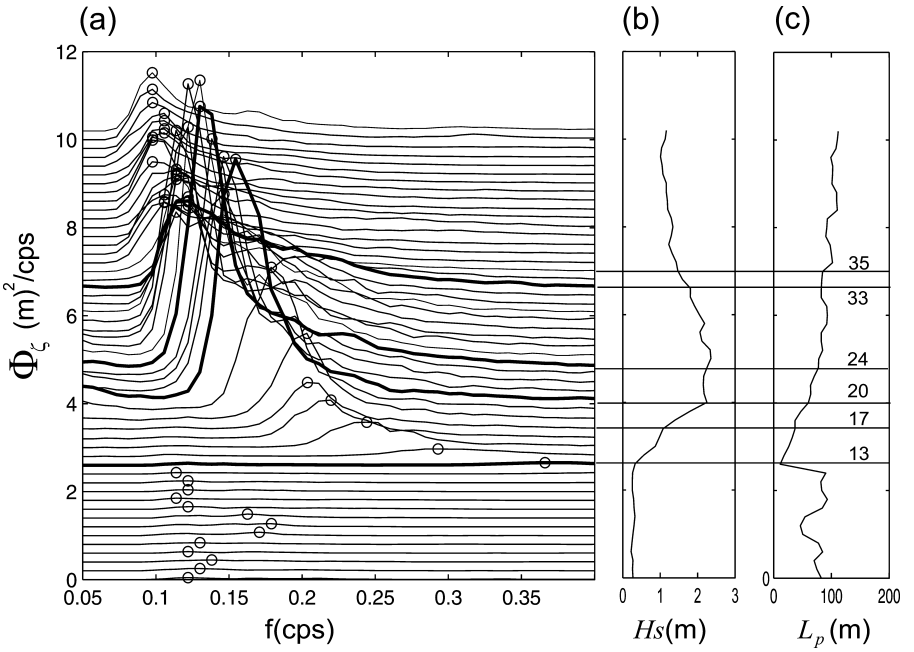

Figure 5. (a) Waterfall plot Φ_ς of surfacewave displacement spectrum ς as a function of frequency over the range accessible to the observations. A circle marks the spectral peak. Each spectrum is offset by 0.2; time increases upward. (b) Significant wave height Hs and (c) spectral peak wavelength L_p. Highlighted records in (a) are those discussed in detail in Section 3; for clarity, Records 17 and 35 are not highlighted.

mean speed from the lowest VADCP bin), and convective velocity $w_* = (B_o H)^{1/3} = (g(\rho_o c_p T_o)^{-1} Q H)^{1/3}$ (defined only when $Q > 0$). All four are of similar magnitude until Record 13, after which u_{S0} greatly exceeds the others (note log scale) until approximately Record 45.

The ratio $-H/L_{MO}$, where $L_{MO} \equiv -u_*^3/\kappa B_o$ with von Kármán's constant $\kappa = 0.41$ is the Monin-Oboukov length scale, exhibits a diurnal cycle both before and after the event (Fig. 4f). However, only after the event do nighttime values exceed +5, a level deemed sufficient to drive the atmospheric boundary layer (absent Langmuir forcing) to the convectively dominated state (Holtslag and Nieuwstadt, 1986). Throughout the LS event, $-H/L_{MO}$ is small and approximately constant (as a result of the constancy of both $B_o \propto Q$ and u_* seen in Fig. 1).

Figure 4g summarizes two characteristics of waves at the peak of the surface displacement spectrum. The start of the LS event in Record 13 is marked by an abrupt decrease in phase speed, c_p, as peak displacement shifts from low frequencies associated with incoming swell to high frequencies of locally generated "young" seas. The evolution described by this metric is seen in more detail in Figure 5, a waterfall plot of surface wave displacement spectra with

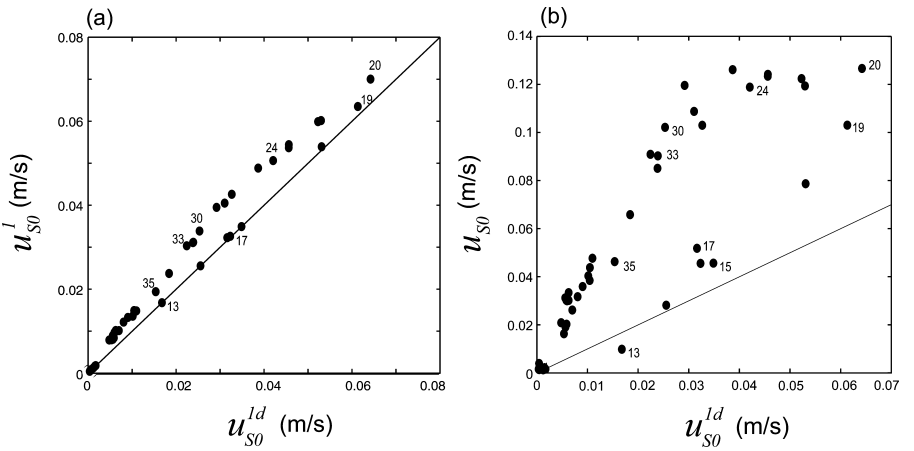

Figure 6. (a) Single-wave surface Stokes drift velocity u_{S0}^{1} versus the deepwater limit u_{S0}^{1d}. During early stages of the wind event, surface Stokes drift velocity moves upward along the 1/1 line that defines the deepwater limit. Departure from this limit, a reasonable definition of waves "feeling bottom," occurs first in Record 20, the start of the LS event. (b) The same plot, but using surface spectral Stokes velocity u_{S0} in place of the single-wave approximation u_{S0}^{1}.

time increasing upward, accompanied by time series of *Hs* and peak wavelength L_p. At the start of this period, existing surface swell has long wavelength but small amplitude. As wind stress increases in Record 13, the displacement peak abruptly shifts to high frequency (short wavelength), subsequently sweeping downward in frequency and increasing in amplitude with time. After Record 20, *Hs* (Fig. 5b) remains approximately steady through Record 30 then falls as the spectral shape flattens (see highlighted spectrum for Record 33), while peak wavelengths continue to increase slowly until the end of the session. While the general character of the temporal evolution of growing seas is familiar, it is notable that wave age c_p/U_{10} achieves the value of 1.2 usually assigned to "fully developed seas" almost immediately after the wind stress increases and retains that value throughout the event (similar evolution is seen if wave age is defined with u_* in place of U_{10}).

Onset of the prototype LS event occurs at a time when locally generated surface wind waves first "feel bottom," defined simplistically by departure of single-wave Stokes velocity $u_{S0}^{1} = a^2\omega_p k_p \cosh 2k_p H/(2\sinh^2 k_p H)$ from the deepwater approximation $u_{S0}^{1d} = a^2\omega_p k_p$, marking transition from deepwater to intermediate type. Single-wave values in Figure 6a are computed with wavenumber $k = k_p$ associated, through the complete dispersion relation, with peak frequency $\omega = \omega_p$ of the observed displacement spectrum, and amplitude $a = \sqrt{2} < \varsigma^2 >^{1/2} = Hs/2\sqrt{2}$.

Concentrated at the origin are Records 0–12, dominated by swell of intermediate type but small amplitude. After the start of the wind event, as peak frequency decreases and amplitude increases (Fig. 5), Records 13 through 19 march up the 1/1 line that denotes

deepwater character. The first deviation of u^1_{S0} from u^{1d}_{S0} occurs in Record 20, coinciding with the start of the LS event. Since a^2 is either approximately constant or decreasing over the remainder of the period, while ω_p and k_p continue to decrease (Fig. 5), u^1_{S0} subsequently decreases steadily, while remaining off the deepwater relationship.

As noted above, *Hs* stops growing after Record 20, suggesting that once surface waves "feel bottom," bottom stress balances surface wind stress, leaving none for wave growth (Gargett and Grosch [2014] indeed document a balance between u_* and u_{*H} during the supercell event). This effect of the bottom may be why surface waves appear "fully developed" early in the event and remain so throughout. If so, this is a major difference from the deepwater case, where surface stress can only be balanced by growth of waves, currents or both.

Although useful as a simple definition of surface waves "feeling bottom," the single wave approximation of surface Stokes velocity in fact behaves only generally like u_{S0}, the spectral version associated with the full surface wave spectrum. As shown in Figure 6b, u_{S0} grows faster than the single-wave approximation during the initial growth phase (Records 13 to 19/20), then remains relatively constant during the LS event. During this latter period, observed (Fig. 5b) decrease in the peak wave amplitude used in u^1_{S0} and u^{1d}_{S0} is apparently compensated by "filling out" of the spectrum at the higher frequencies/wavenumbers (see highlighted spectra for Records 24 and 33 in Fig. 5a) that are more highly weighted in calculating spectral Stokes velocity.

c. Mean and turbulent flow structure

Figure 7 presents detailed images of six records chosen to illustrate distinct stages in evolution of the prototype LS event. These stages were chosen on the basis of features in the backscatter field, features that are, not surprisingly, closely linked to distinctive features of the velocity field and the processes forcing it. Because horizontal mean flows are important to the discussion of the event as a whole, these figures depict total, not fluctuation, horizontal velocities. For each record, the highly characteristic backscatter field will be discussed first, followed by the associated velocity fields. The range of A is fixed to allow relative comparisons, while offset is chosen to reveal the maximum detail possible. Scaling of the vertical velocity field is fixed (± 0.04 m s^{-1}) throughout to allow direct comparison between individual records. To enable similar comparison of horizontal shears, the horizontal velocity scale range is fixed at 0.4 m s^{-1}, while varying offsets allow for the large changes in mean velocities observed over the event. Horizontal velocity fields are shown above the standard level of potential sidelobe contamination (dotted line) because in some cases—for example, Record 24 in Figure 7d—this contamination appears suppressed, presumably because of the presence of high near-surface bubble concentrations "masking" the surface in the sidelobe.

At the start of Record 13 (Fig. 7a), surface layer backscatter is high but quite uniform. However, by record end, backscatter has developed the sharp downward small-scale structures usually associated with bubble clouds carried downward by LC (Zedel and Farmer,

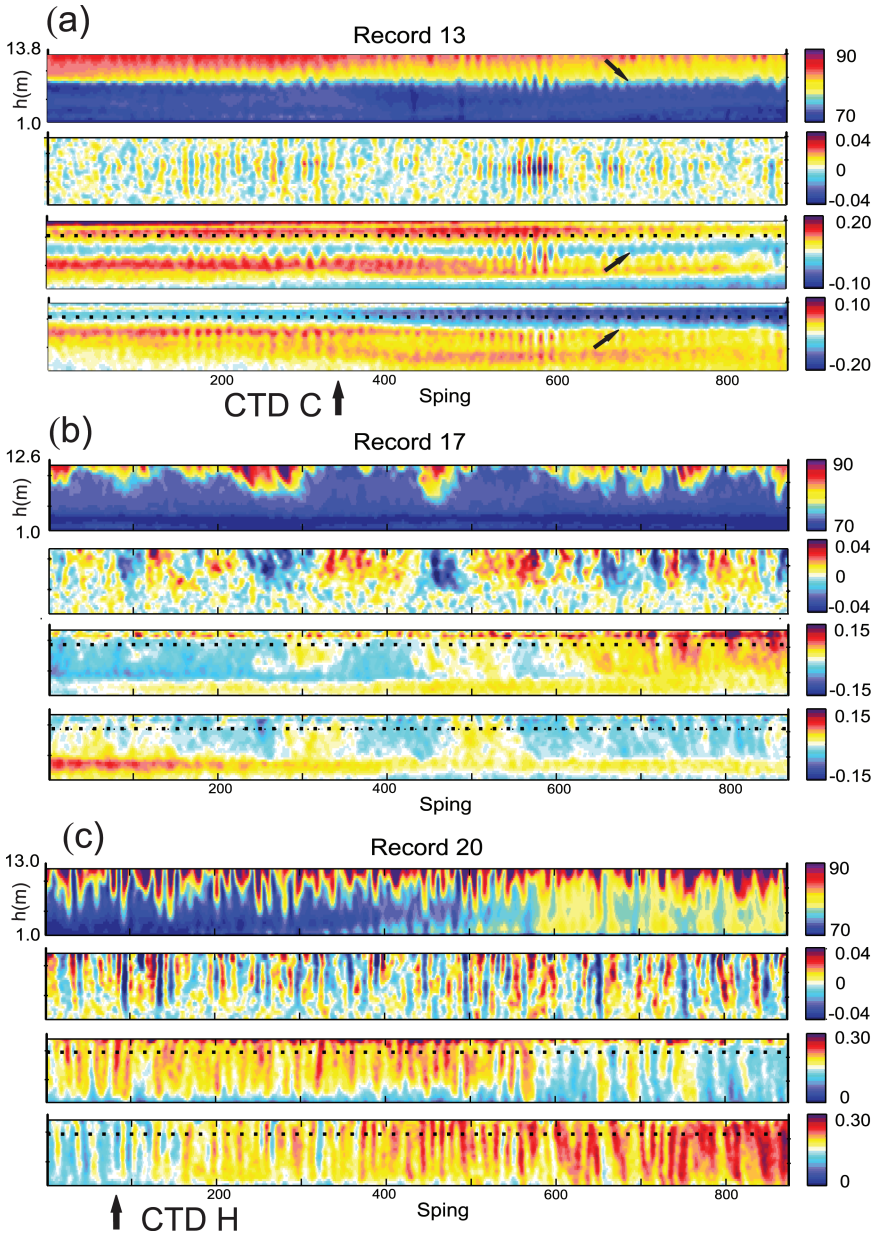

Figure 7. Imaged backscatter and velocity fields for Records (a) 13, (b) 17, (c) 20, (d) 24, (e) 33 and (f) 35. In each record panel, the upper image is backscatter amplitude A with range fixed at 20 units; changes in total backscatter require different lower bounds. Below A is vertical velocity w', with fixed scale range of ± 0.04 m s^{-1}, followed by downwind velocity u_1, then (bottom) crosswind velocity u_2. To normalize visual comparisons of shear, the velocity scale range of both u_1 and u_2 is fixed at 0.30 m s^{-1}: only the lower bounds change to accommodate different mean flows. The bottom of the lowest bin is at $h = 1$ m; height of the top of the uppermost available bin is noted on the A height axis. On both horizontal velocity images, dotted horizontal lines mark the height above which estimates of these velocities may possibly be contaminated by sidelobe effects, although the observed height of contamination is often higher in the water column, depending on the density of near-surface scatterers masking the surface. Subsampled ping number Sping = time(s)/10.

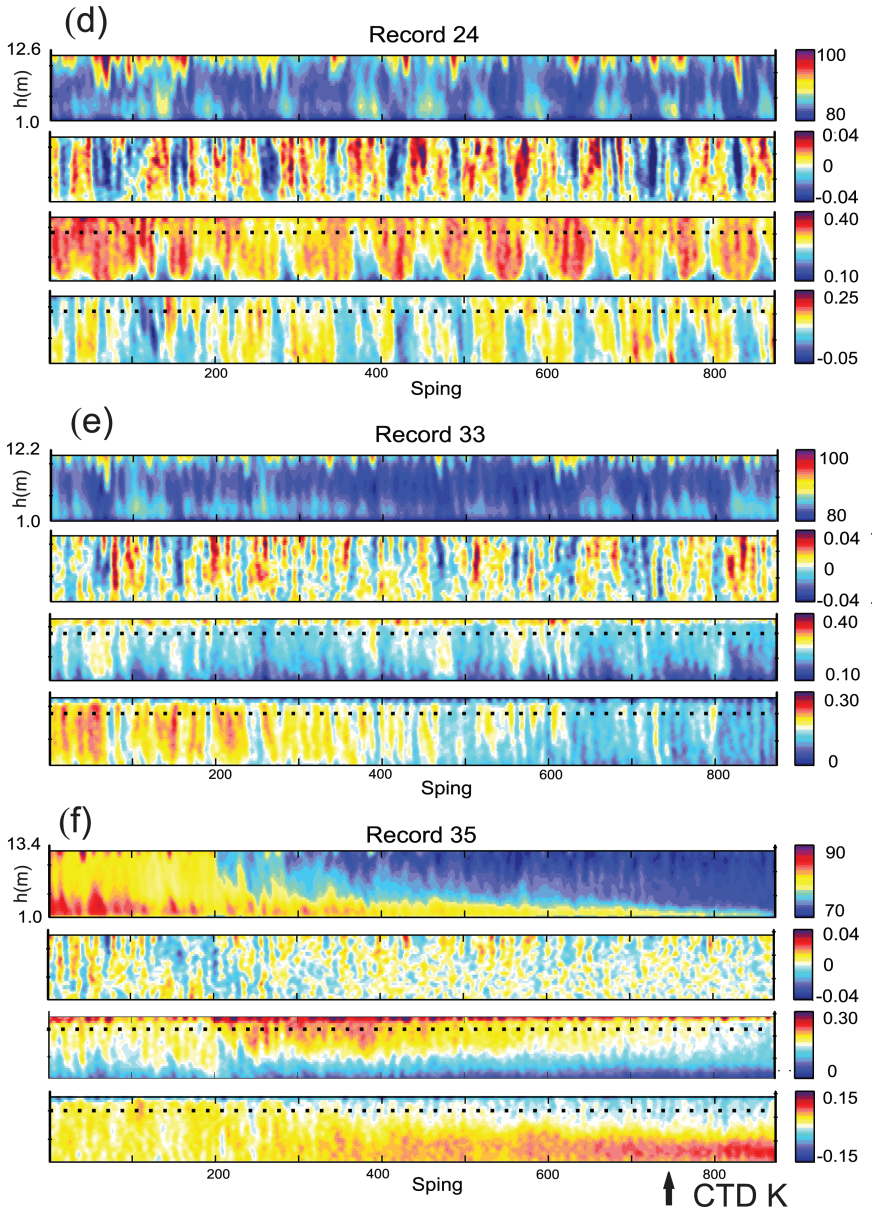

Figure 7. (continued)

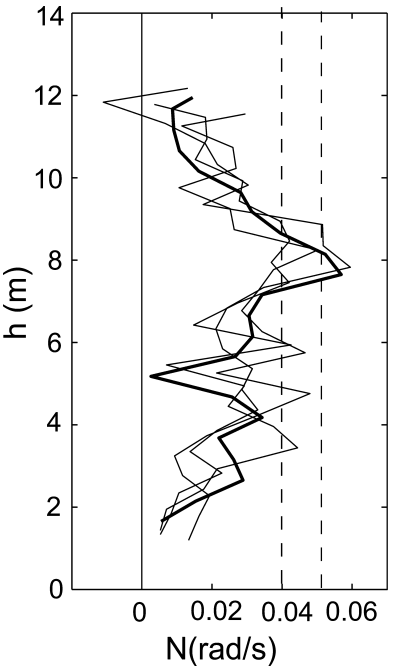

Figure 8. Profiles of buoyancy frequency N computed from four CTD profiles taken during Record 13. CTD C (highlighted) was taken near the middle of Record 13. The vertical dashed lines denote a range of apparent frequencies determined by period-counting of two "groups" in Figure 7a.

1991). These signatures are confined to a surface layer with a base ∼7–8 m above bottom (delineated by arrows) that is associated with transition from high to low backscatter and coincident transition from the low density gradient surface layer to the linearly stratified interior (CTD C). Vertical shear at the surface layer base increases markedly during this record, predominantly through increase in u_2. The accelerating surface layer crosswind flow is shoreward ($u_2 < 0$), consistent with Ekman transport to the right of the (northeasterly) wind, hence with initial stages of coastal setup leading to downwelling. We argue that the increased shears leading to the deepening events in Figure 3 are associated with wind-driven setup of a cross-shelf pressure gradient, and speculate that the final disappearance of stratification may be associated with offshore movement of a downwelling front.

At the time of Record 13, w' is small near surface, but sporadically larger and highly vertically coherent within the stratified interior. Maximum values occur just below the surface layer base, as expected of first mode internal waves at the buoyancy frequency. As seen in Figure 8, estimates of apparent frequency associated with these motions are approximately equal to the column maximum buoyancy frequency computed from CTD profiles taken during Record 13, suggesting that these are internal wave motions forced by surface layer LC impinging on the top of the stratified interior, as modelled by Polton et al. (2008).

Over the next several hours, the faint backscatter features seen in the upper layer of Record 13 develop into stronger features, with high surface layer backscatter clouds in Record 17 (Fig. 7b) now clearly associated with negative (downwelling) vertical velocities. These signatures are still confined to a surface layer bounded below by a region of shear in the two horizontal velocity components at ∼4 m. Deepening of the shear layer from its original position at ∼7–8 m in Record 13 occurred during Record 15, beyond which it remained at constant height until midway through Record 19, when it again began to deepen. The last vestiges of vertical shear disappear at Subsampled ping number Sping ∼ 600 in Record 20 (Fig. 7c), presumably coincident with complete disappearance of the weak density structure seen in CTD H (CTD profiling was suspended after this point because of deteriorating surface conditions). This point marks both the onset of coherent velocity structures spanning the water column and the first appearance of bottom-origin backscatter clouds that overlap those originating from the surface.

Record 24 (Fig. 7d) is from the middle of the period of near-steady wind forcing from Record 20 through 30. Throughout this period, bottom-origin backscatter increases in magnitude (note the larger lower bound of backscatter range in Fig. 7d,e), and the three-dimensional velocity fields exhibit the strong phase relationships characteristic of full-depth LC. Downwellings/upwellings are associated with increased/decreased downwind flow, particularly near the bottom, and a change in sign of near-bottom crosswind flow (dependent on crosswind mean flow direction at the time) in the middle of downwellings, the opposite change in upwellings. These phase relationships are seen more clearly in the mean-removed presentations of Gargett et al. (2004) but are still evident in the mean-included fields of Figure 7.

Starting around Record 33, the LS begin to weaken. In Figure 7e note decreasing magnitude of horizontal velocity fluctuations and a decrease in the vertical extent of both surface-origin and bottom-origin backscatter clouds. Finally, full-depth backscatter disappears within Record 35 (Fig. 7f), coincident with re-establishment of the diurnal heating and cooling cycle (Fig. 4f). Since the event ends at a time when surface flux is destabilizing, it is clear that event cessation is not due to onset of stabilizing surface buoyancy flux. Also coincident is reappearance of vertical shear in both horizontal velocity components, accompanied by weak density stratification (CTD K). The reappearance of shear and weak stratification is undoubtedly related to the weakening of wind/wave forcing that starts in Record 33, as winds decrease in magnitude and swing toward W from SW. The shift in direction ends support for the cross-shelf pressure gradient that had produced approximately shore-parallel geostrophic flow during the near-constant NE winds of the LS event, allowing rotation-influenced gravitational adjustment of locally well-mixed water columns. The sharp decrease in LC growth rate g_* (Fig. 4c) associated with the same weakening wind/wave forcing apparently leaves full-depth LS unable to prevail against even weak stratification.

The importance of water column stratification in determining the depth achieved by LC under declining wind/wave forcing is reinforced by strong correlation between

stratification and sporadic re-appearance of weaker full-depth structures in the aftermath of the LS event (Records 37–40 and 49–51; see Fig. 1a and b). As discussed above, the erratic stratification observed after the LS event (Fig. 2c) likely results from geostrophic adjustment of vertically well-mixed but horizontally nonuniform water masses. While CTD K exhibits three-layer stratification, CTD L (taken during Record 40) again has no interior stratification. The assumption that this change actually occurs near the beginning of Record 37 would explain the reappearance of weak full-depth backscatter in Records 37 through 40 (Fig. 1a). CTD L is followed by three stratified profiles, M in Record 42, N in Record 44 and O in Record 46, during which backscatter is again relegated to separated surface and bottom layers (Fig. a). The final CTD (P, in Record 48) reverts to weak stratification, again coincident with initiation of weak full-depth velocity and backscatter signals through the end of the period. Interpretation of Record 48 is complicated by the possibility of convection, since $-H/L_{MO} > 5$ at the time; however, in Records 49–51, heat flux is again stabilizing, suggesting that the observed fluctuations are in fact weak LS.

4. Requirements for a LS event

In this section, we first define the conditions necessary for existence of full-depth LC, then demonstrate that they coexist with conditions under which sediment resuspension occurs, guaranteeing a supply of material for the bottom-origin backscatter clouds that clearly reveal LS events on the shallow shelves off the U.S. East Coast.

a. Requirements for full-depth LC

LS events involve the coincidence of full-depth LC with a supply of resuspended sediment. The following subsection will demonstrate that sediment is available at the time LC achieve full depth, hence here we use the terms "full-depth LC" and LS interchangeably. From the above examination of the prototype event, it is clear that one essential requirement for existence of full-depth LC is a water column that is unstratified (or nearly so; a definition of "nearly," which must certainly depend on the level of surface forcing, is outside the scope of this paper but warrants further investigation). Present observations indicate that LS events are associated with very weak linear stratification, O(0.005 kg/m^4), a value that will be used to define an "unstratified" water column. Unstratified conditions at the inner shelf location of LEO15 are normally associated with downwelling winds and surface buoyancy fluxes that are destabilizing or at most weakly stabilizing, conditions occupying a significant fraction of the annual cycle, from early fall through late spring (Kohut et al., 2004). This is also true of inner and mid-shelf regions of the South Atlantic Bight (Blanton et al., 2003), as well as the inner shelf in the wintertime Gulf of Mexico, providing ample habitat for LS. Upwelling winds, generally weaker in magnitude, are associated with stratified conditions at LEO15, suggesting that any upwelling front, should one exist, lies inshore of 6 km.

Provided an unstratified water column, LS are observed only when surface wind/wave/buoyancy forcings lie within specific ranges of the two nondimensional parameters *La* and

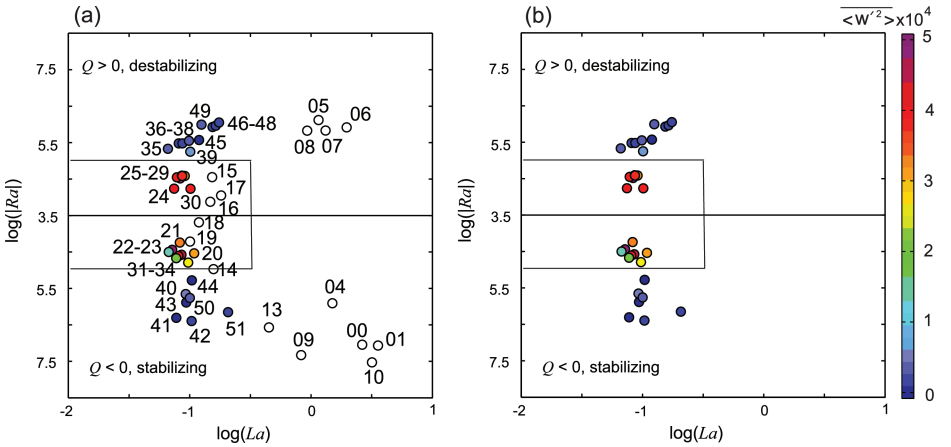

Figure 9. (a) All available records from the prototype event, plotted in the (logarithmic) plane of two parameters La and $|Ra|$ defined by Gargett and Grosch (2014), who examined only records with destabilizing surface buoyancy forcing (upper half-plane). The mirror-image lower half-plane is a similar plot for records with stabilizing buoyancy flux. Color codes indicate $\overline{< w'^2 >}$ in $(\mathrm{m\ s^{-1}})^2$ for acceptable records (see definition in text); unacceptable records, where $\overline{< w'^2 >}$ may be due wholly or partially to internal waves, are not color-coded. (b) Acceptable records only. LS records are the high variance records, with $\log(La) \sim -1$ and $\log|Ra| < 5.0$. In both panels, the upper box denotes the range in which Gargett and Grosch (2014) found LS structures for records with $Q > 0$. The mirror image box contains all LS records with $Q < 0$, generalizing the results of Gargett and Grosch (2014) to both signs of surface buoyancy forcing.

Ra. In Figure 9, the top half of each panel is the plane used by Gargett and Grosch (2014), who considered only cases with destabilizing surface heat flux. Here, the mirror image plane on the bottom half of each panel allows inclusion of records with stabilizing surface heat flux. Figure 9a includes all available records from the May period, while Figure 9b contains only "acceptable" records, those in which $\overline{< w'^2 >}$ is not contaminated (as it is, e.g., in Record 13) by vertical velocities associated with internal waves. Lacking continuous CTD density data, a record is defined as "acceptable" when the continuously measured top-to-bottom temperature difference $\Delta T < 0.5°\mathrm{C}$, a value corresponding to buoyancy period longer than the record length when using the mean T/S relationship before the event. For this and smaller values of ΔT, w' calculated by removing linear least squares fits over record length will be uncontaminated by internal wave vertical velocities, and $\overline{< w'^2 >}$ can be unequivocally interpreted as turbulent variance. In Figure 9a, color codes indicate $\overline{< w'^2 >}$ of acceptable records; unacceptable records are plotted as unfilled circles. All the LS records (20 through 34) lie within the region $\log|Ra| < 5.0$ and $\log(La) < -0.5$ identified as necessary for LS by Gargett and Grosch (2014) on the basis of a much broader data set.

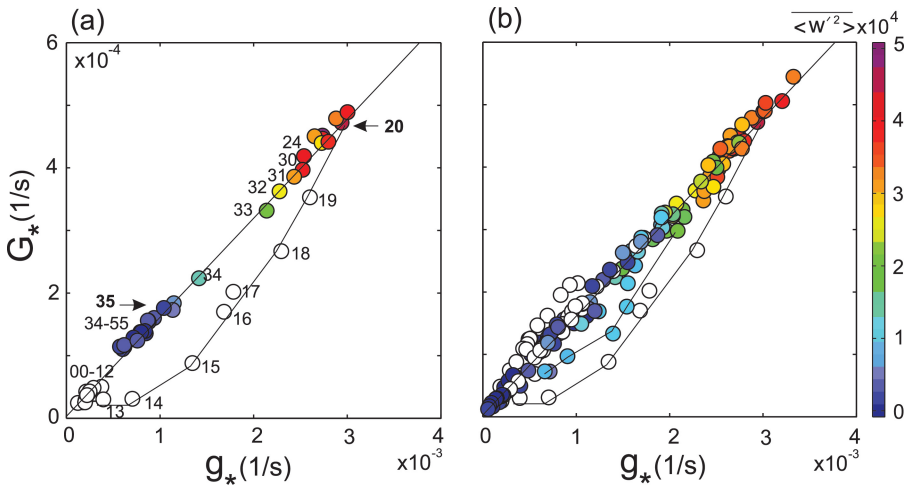

Figure 10. (a) Near-bottom ($x_3 = -0.9H$) LC growth rate G_* versus near-surface ($x_3 = -0.2H$) growth rate g_* for the prototype event. Acceptable records are color-coded by magnitude of $\overline{< w'^2 >}$ in $(\text{m s}^{-1})^2$. Only those records (13–19) with deepwater surface waves early in the storm event lie off the linear fit shown. The LS event starts in Record 20 and ends in Record 35. (b) Available records from three LS events. The outer black curve is the May event of (a); the inner black curve is a similar situation in the early stages of the October event. All other records from October and September LS events lie along the same straight line drawn in (a).

It may seem puzzling that the existence of coherent full-depth structures apparently depends on a parameter (Ra) that involves only near-surface Stokes shear. Once surface waves "feel bottom," Stokes shear extends throughout the water column and hence can contribute to LC generation via the C-L vortex forcing term at all depths, not just near the surface. One might thus rather surmise that deep Stokes shear (or more completely, a LC growth rate G_* determined near the bottom) might be as, or more, relevant to full-depth structures. In this regard it is illuminating to examine very distinctive relationships observed to exist between growth rates evaluated near-surface $g_*(x_3 = -0.2H)$ and near-bottom $G_*(x_3 = -0.9H)$ (note that Stokes shear at $x_3 \equiv -H$ is zero). As seen in Figure 10a, growth rates are essentially zero at both depths when the May wind event begins in Record 13. As seas build up, near-surface Stokes shear, hence g_*, increases first, followed by deep Stokes shear. G_* increases relative to g_* until, in the same record that surface waves first depart from deepwater character, it reaches a quasi-linear relationship with g_* that persists both during and after the event. Figure 10b shows that two other LS events (discussed further in Section 5) reach the same linear relationship, with trajectories that differ only in the early stages of an event, depending on existing wave state when wind stress forcing first increased. The October LS event follows a curve different from that of the May event but reaches the same linear relationship, while that of the September event starts from an existing intermediate wave state, hence lies on the linear relationship throughout.

The general behavior observed during initial wave growth from a deepwater state is intuitive; growth rates increase first near surface, then eventually at greater depths. While less intuitive, the subsequent quasi-linear relationship may be explored by considering the ratio of near-bottom single-wave Stokes shear to that near surface, which in the limit of very long (shallow-water) waves is given by

$$\lim_{kH\to\infty}\left(\frac{\sinh(2k_p(-0.9H+H)}{\sinh(2k_p(-0.2H+H)}\right)=\frac{0.2k_pH}{1.6k_pH}=\frac{1}{8}. \tag{4}$$

Since stress-driven mean shear is parameterized by u_*/H at both boundaries, this limit corresponds to a growth rate ratio of $G_*/g_* = \sqrt{1/8} = 0.35$. That the straight line drawn in Figure 10 has a somewhat different slope (0.16) is not surprising: the dominant waves did not achieve the shallow-water limit used above, and moreover, as demonstrated in Figure 6b, the wave field is not fully characterized by a single-wave assumption. Regardless, once surface waves achieve intermediate character, a quasi-linear relationship between near-bottom and near-surface LC growth rates is observationally, if not theoretically, well established by the data of Figure 10. If, as we will argue in Section 6, G_* is an important determinant of the strength and organization of full-depth LC, this relationship suggests that any dynamically relevant threshold in g_* (the growth rate that enters Ra) is associated with a similar threshold in G_*, accounting for success of Ra in predicting the occurrence of full-depth LC.

In summary, necessary and sufficient conditions for the occurrence of LS are unstratified water columns and wind/wave/buoyancy forcing within a known range of the nondimensional parameters La and $|Ra|$. In addition, there is a less well defined requirement that turbulence produced at the bottom boundary by pressure-gradient–driven currents like tides be sufficiently weak. Using quadratic bottom-stress velocity u_{*H}, Gargett and Grosch (2014) defined a "bottom stress Langmuir number" $La_H = u_{*H}/u_{S0}$, similar to La. Using a data set that included the May event, they tentatively concluded that records with $La_H/La < 2$ are essentially unaffected by turbulence generated in the bottom boundary layer. All of the LS records during the May event have $La_H/La \sim 1$, fulfilling this criterion.

b. Requirements for sediment resuspension

As documented in Section 3(b), the prototype supercell event begins at a time when locally generated surface wind waves first "feel bottom." This may also be considered as the first time the bottom "feels the waves," with development of a thin (Trowbridge and Agrawal, 1995) wave boundary layer that allows the necessary transition from zero flow at the bottom to nonzero but nearly irrotational surface wave velocities in the interior. The strong shear of this thin wave boundary layer is a major agent of sediment resuspension.

The dashed line in Figure 11a is the component of bottom stress velocity due to surface waves: $u_*^w = (\tau_w/\rho_o)^{1/2}$, where $\tau_w = 0.5\rho_o f_w < u_w^2 >$ is calculated from record-averaged values of surface wave horizontal velocity variance $< u_w^2 >$ at the bottom (derived from the displacement spectrum obtained from vertical velocity measurements, see Gargett and

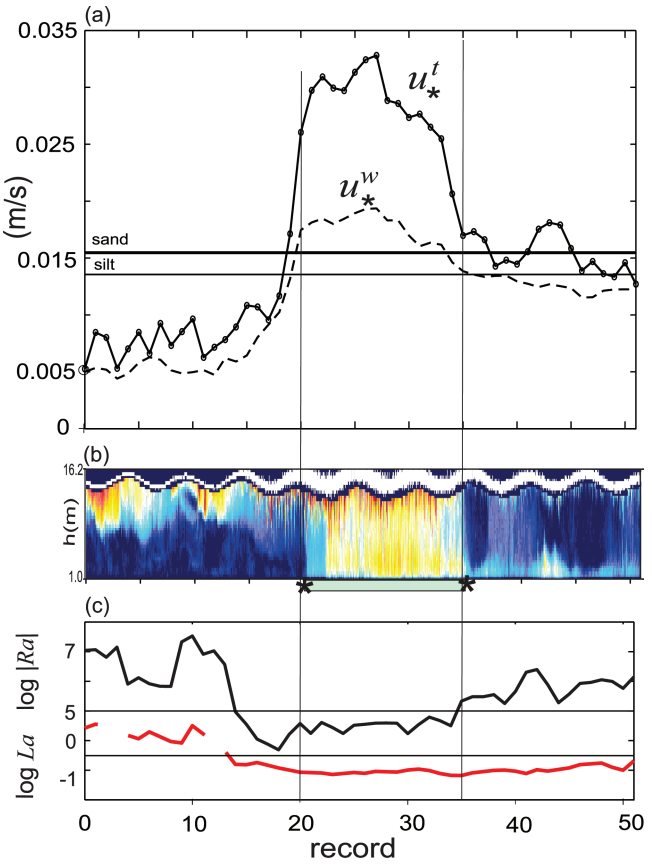

Figure 11. (a) Time series of record mean values of surface wave bottom stress velocity u_*^w and total (wave plus current) bottom stress velocity $u_*^t = u_*^w + u_{*H}$. Horizontal lines mark suspension thresholds for size categories corresponding roughly to silt (60 μm) and sand (388 μm). (b) Backscatter image of the prototype May event.The green bar indicates the period when the water column is unstratified; stars (and vertical lines) at Records 20 and 35 mark the start and end of the LS event. (c) Time series of (logarithmic) values of the scaling parameters $|Ra|$ (black line) and La (red line). Horizontal lines denote the values $\log|Ra| = 5$ and $\log La = -0.5$ defined by Gargett and Grosch (2014) as critical to the existence of LS in an unstratified water column. Missing values of La are records in which Stokes velocity is not well determined.

Grosch [2014]) using the drag coefficient f_w of Soulsby (1997, his eqn. [62a]) computed for a flat bed with maximum grain size that of sand). Assuming wind and current are roughly aligned, as is the case in LS events, the total bottom stress velocity (solid line) is $u_*^t = u_*^w + u_{*H}$; both components rise rapidly at storm onset. Comparing with threshold values for sediment motion computed with grain size and observed bottom temperature using the Shields (1936) diagram as modified by Madsen and Grant (1976), Figure 11a

shows that u_*^w alone exceeds values sufficient to resuspend first silt, then sand, within Record 19. When the mean flow contribution is added, the thresholds are first exceeded in Record 18. Initially available in a thin near-bottom layer, resuspended sediment will only appear in the observed part of the water column (above $h = 1$ m) when distributed higher by some type of turbulent structure that engages this layer, here by the LC that fill the water column when stratification disappears in Record 20 (the other two necessary conditions for LS, $|Ra| < 10^{-5}$ and $La < \sim 0.3$, having been achieved while the water column was still stratified; see Fig. 11c).

During the prototype LS event, *Hs* remains relatively constant, and dominant wavelength increases only slowly (Fig. 5b), hence the wave stress component u_*^w also remains relatively constant. However, the component due to the strong mean flow associated with LS events (Gargett and Wells, 2007; Tejada-Martínez and Grosch, 2007) continues to rise until it contributes ∼30% of the total. Starting about Record 30, both components decrease, with the mean component decreasing the more sharply. Total bottom stress velocity nonetheless remains above or near the silt resuspension threshold throughout the remainder of the period, more than a day during which the backscatter signal shows periodic evidence of sediment within the water column (Fig. 1). During Records 41–45, the mean component increases sufficiently that total bottom stress velocity again surpasses sand as well as silt thresholds, suggesting that coincident increase in bottom-origin backscatter amplitude during this period is caused by the presence of a wider size spectrum.

The time series of measured bottom stress velocities seen in Figure 11 is consistent with both availability of sediment when it is observed in bottom-origin backscatter and lack of availability during the nearly 2-day period preceding the event, when no bottom-origin backscatter is seen within the observed water column.

5. Conditions associated with onset and cessation of LS events

While focus thus far has been on complete description of a single prototype LS event, consideration of additional events is desirable in order to verify common requirements for the developmental cycle. At LEO15, LS events are increasingly rare in late spring and completely absent during summer months (June, July, August), when winds are generally from the south and stratification is large due to both increased solar insolation and upwelling-favorable wind direction. After late-summer decrease in insolation and seasonal change in direction of winds to downwelling-favorable, LS events become common. However, increased frequency of synoptic wind events during the remaining months of available measurements (September and October) makes it difficult to find isolated events like the prototype; in particular, conditions at the start of an event are frequently influenced by those of a previous wind/wave episode. Only two additional events seemed separated sufficiently (defined, rather arbitrarily, as 10–12 hours of low and variable winds) from previous conditions to be usefully compared with conditions characteristic of the prototype. Various defining fields associated with these two events, one in October (Fig. 12) and the other

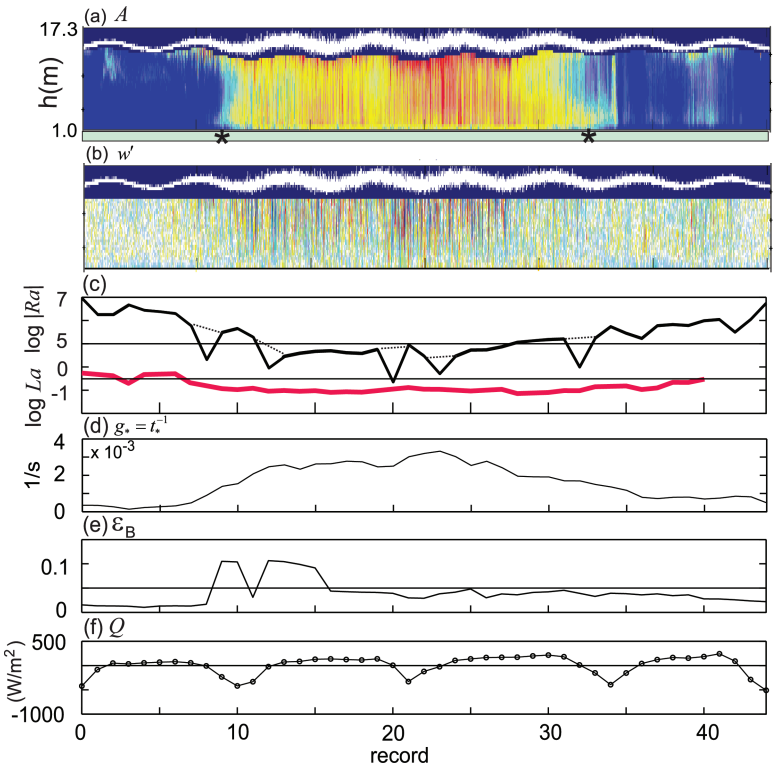

Figure 12. The LS event in October. (a) A and (b) w' (± 0.04 m s^{-1}), along with surface height (white lines), are determined from the vertical beam of the VADCP. Green bar denotes the period of time when the water column was unstratified; stars denote the start and end of the event. (c) Logarithmic variation of $|Ra|$ and La. Interpolated (dashed) values of $|Ra|$ are shown for records with surface heat flux Q near zero, as a result of averaging over a period when Q changes sign. Missing values of La are records in which Stokes velocity is not well determined. Horizontal lines denote the values $\log|Ra| = 5$ and $\log La = -0.5$ defined by Gargett and Grosch (2014) as critical to the existence of LS in an unstratified water column. (d) Langmuir circulation growth rate g_*. (e) Surface wave breaking parameter ε_B. (d) Surface heat flux Q. Records are approximately 2.4 h in length.

in September (Fig. 13), allow comparison of conditions associated with the start and end of these additional events with those of the prototype. The October event is most similar to the prototype, both beginning and ending abruptly. In contrast, the September event requires nearly a full day after winds increase and surface-origin bubble clouds indicative of LC appear in order to achieve bottom-origin and surface-origin backscatter features that consistently overlap in the vertical.

The starts of all three events are associated with increasing LC growth rate g_*. Like the prototype event, growth rate increase in the October storm (Fig. 12) is relatively abrupt and roughly coincident with onset of surface wave breaking as predicted by $\varepsilon_B > 0.05$. However,

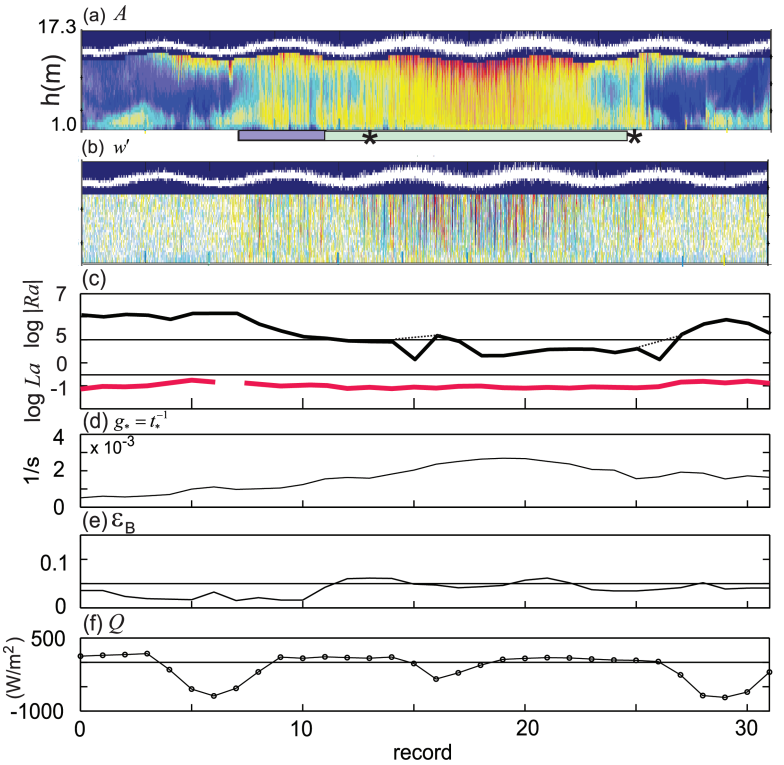

Figure 13. The LS event in September. The purple bar below the backscatter panel denotes uncertainty in time of disappearance of stratification, which occurs sometime between CTDs in Records 7 and 11. Otherwise, fields are as described in the caption to Figure 12.

in the September storm (Fig. 13), wave breaking is clearly evidenced by surface-origin bubble clouds in Record 4, many hours before ε_B exceeds 0.05 in Record 11. Either wave breaking is not, after all, a determinant of strong LC growth, or a more complex breaking metric is needed (Banner et al., 2002).

Although not shown, in all three cases surface waves achieve intermediate type, and resuspension thresholds for the full sediment size spectrum are exceeded either well before or concurrent with times at which LC are observed to reach the bottom. In the October event, the resuspension threshold for the full size spectrum is exceeded in Record 12; stress falls below that required to resuspend sand in Record 36 and silt in Record 40. Surface waves are of intermediate type throughout the September period, as a result of a previous wind/wave event. Moreover, total bottom shear stress is large enough to resuspend some or all of the silt/sand size spectrum throughout the period (note the appearance of bottom sediment clouds during maximum tidal flows both before and after this event). In both

cases, resuspended sediment is available whenever all additional conditions necessary for full-depth LC are met.

We thus argue that LS events start when the three conditions for full-depth LC outlined in Section 4(a) (unstratified water columns, $La < \sim 0.3$, and $|Ra| < 10^5$) are met, but note that these conditions are not necessarily fulfilled simultaneously. In the prototype event, which starts with strong stratification, the LS event is initiated in Record 20 by the last condition to be met, that of an unstratified water column. The October event (Fig. 12) starts from a state with no stratification and $La \sim 0.3$, with La falling definitively below 0.3 in Record 7. Here the LS event is initiated when $|Ra|$ falls below 10^5 somewhere near Record 10. The September event has a much less definite start. While bottom-origin backscatter clouds and full-depth velocity structures can be observed intermittently beginning in Record 8, they wax and wane until, sometime around Records 13–14, values of $|Ra|$ that have remained near 10^5 fall below 10^5. LS structures appear consistently only past this point. In this case, lack of certainty about exactly when stratification disappears—the water column was stratified in a CTD taken during Record 7, and unstratified by the next CTD in Record 11—precludes identifying the start of this event solely with meeting the condition on $|Ra|$.

The end of LS events is obviously associated with decrease in wind stress at the end of a storm and the consequent, though slower, decrease in the surface wave field. However, a number of potential mechanisms exist (and may coexist). In addition to failure of any one of the three conditions for LS, two other possibilities are cessation of surface wave breaking (if breaking indeed provides a more efficient mechanism for generation of LC) and increase in magnitude of the surface buoyancy (heat) flux; we address these first.

In all three events documented, the dominant wave breaking parameter ε_B falls to its threshold near the time an event ends but continues to hover very near it for often substantial periods afterward, as a consequence of the slow decay of the dominant surface waves. This behavior makes it unlikely that the often-abrupt ends of LS events are associated with breaking cessation.

As noted in Section 3(a), LS events are characterized by reduced surface buoyancy (heat) fluxes. At an event end, the normal diurnal cycle may resume with either sign of the heat flux: if stabilizing, surface fluxes might weaken LC by inducing stratification, while destabilizing fluxes might do so by interfering with the strong phase relationships characteristic of LC. However, event ends are not associated with a consistent sign of increased heat flux: the September and October events end as Q becomes stabilizing, but the prototype ends with destabilizing Q. While increased |Q| might still be responsible for event ends, the mechanisms involved would differ with sign of Q. We suggest that it is more likely that the end of a LS event occurs when one of the three conditions defined as necessary for event onset ceases to hold and that, as was the case with onset, these conditions do not necessarily cease simultaneously.

For all three events, La remains < 0.3 at the event end (and sometimes substantially beyond it, e.g., Figs. 11 and 13), as a result of the slower decay of waves relative to wind after strong wind forcing. Thus failure of the La criterion is definitely not the cause of

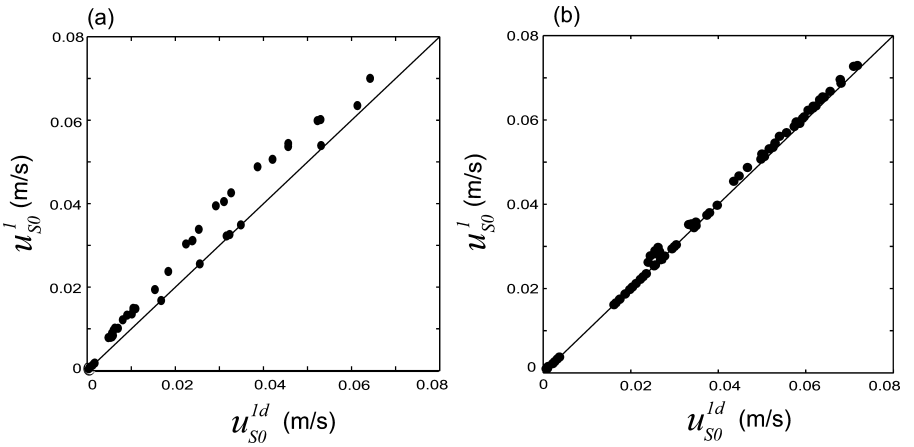

Figure 14. Comparison of single-wave surface Stokes velocity u^1_{S0} to the deepwater limit u^{1d}_{S0}, from LS events at (a) LEO15 (15 m depth, May event) and (b) R2 (27 m depth). Typical storm waves only just achieve intermediate character at R2.

the end of events. Reappearance of stratification is coincident with the end of LS events in the prototype event and the September event. However, in the October event, the water column remains unstratified for several records after event end, which is instead associated with increase of $|Ra|$ to values greater than 10^5 around Record 32. In the other two cases, failure of the $|Ra|$ criterion is roughly coincident with the reappearance of stratification; its fortuitous isolation from any stratification effect at the end of the October event suggests its importance in all cases.

6. How deep?

We now turn to the question of how deep a water column must be before LS events no longer occur. Part of an answer is that LS events will not occur in (unstratified) water columns deep enough that typical storm-driven surface waves do not achieve intermediate character. In all three LS events examined, surface waves are observed to transition from deep-water to intermediate type either before or at event onset. When waves "feel bottom," the bottom "feels the waves," providing resuspended sediment to form the bottom-origin plumes characteristic of LS once LC achieve full depth. Expressed in terms of peak wavenumber k_p, a necessary criterion for LS in unstratified water of depth H is thus that the ratio $R_I \equiv u^1_{S0}/u^{1d}_{S0} = (\cosh 2k_pH/2\sinh^2 k_pH)$ of single- wave Stokes velocities defined previously (Fig. 6) exceeds 1. Figure 14 compares the behavior of single-wave Stokes velocities from the prototype LS event at LEO15 with those calculated from VADCP data taken during a typical storm event at R2, a 27-m-deep mid-shelf location off Georgia characterized by similar sediment type but maximum tidal velocities approximately 2–3 times those at LEO15 (Savidge et al., 2008). Unstratified water columns occur at R2, as at LEO15, as a

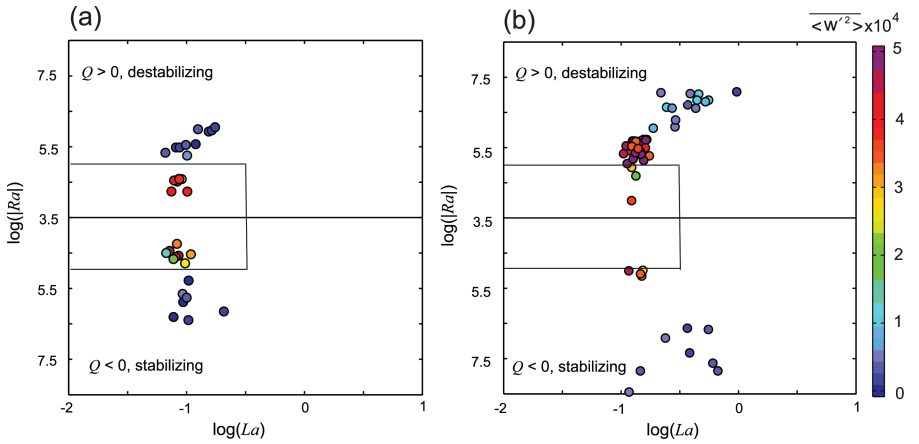

Figure 15. Comparison of the distribution of acceptable records during LS events at (a) LEO15 (15 m depth, May event) and (b) R2 (27 m depth) in the plane of log(La) and log($|Ra|$). R2 records tend to lie near but slightly above the condition $|Ra| < 10^5$ found to ensure LS in the LEO15 observations. Color codes indicate $\overline{< w'^2 >}$ in (m s^{-1})^2.

result of coastal downwelling associated with nor'easter storms. However, typical storm waves at R2 just barely "feel bottom." As documented in Figure 14b, the average value of R_I during a LS event at R2 is only ~4% over the deepwater value of 1, compared with an excess of 20% during that at LEO15.

While intermediate wave type is necessary for sediment resuspension, it is clearly not sufficient for LS; a counter-example is swell, which at the depths of both sites is of intermediate or even shallow-water type, yet does not generate LS. Waves that generate LS in an unstratified water column must not only be of intermediate type but of sufficient amplitude. The necessary combination of these coupled demands on wavelength and wave amplitude is incorporated in the nondimensional parameters La and $|Ra|$. As seen in Figure 15, records from a LS event at R2 have $La \sim 0.1$, as was the case at LEO15. However, because values of both $|Q|$ and t_* are typically larger at R2 than at LEO15, $|Ra|$ tends to lie slightly above the condition $|Ra| < 10^5$ found to ensure coherent LS in the LEO15 observations.

Indeed, although full-depth velocity and backscatter features are observed at R2 during this event, the coherent phase patterns in the three-dimensional velocity field (Gargett et al., 2004) that are defining characteristics of LS observed at LEO15 are present only sporadically (D. K. Savidge et al., pers. comm.). In addition (despite similar sediment types at both locations), bottom backscatter clouds at R2 are more diffuse and less correlated with vertical velocity than at LEO15. Both features are consistent with the behavior described in Section 5 during the early stages of the September LS event at LEO15, where disorganized full-depth structures were observed in an unstratified water column with La ~0.1 and $|Ra|$ just in excess of 10^5, becoming organized LS only when $|Ra|$ fell decisively below 10^5.

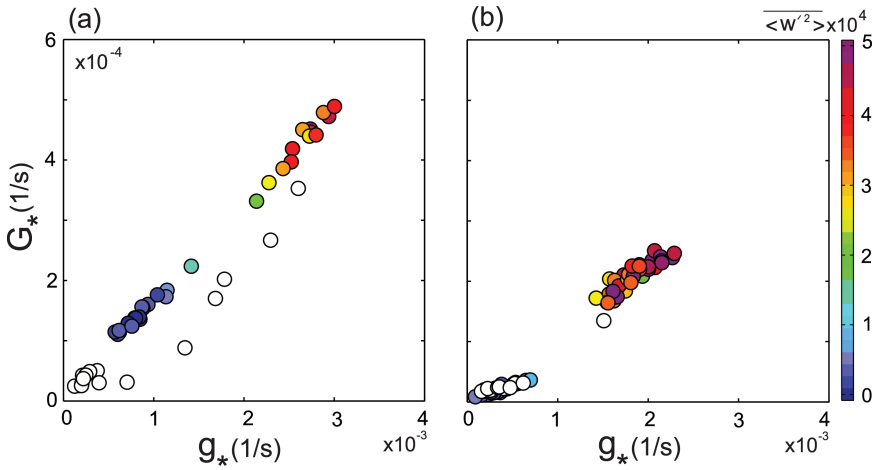

Figure 16. Near-bottom ($x_3 = -0.9H$) LC growth rate G_* versus near-surface ($x_3 = -0.2H$) growth rate g_* for full-depth events at (a) LEO15 and (b) R2. Color codes indicate $< w'^2 >$ in $(\mathrm{m\ s^{-1}})^2$. LC growth rates are smaller at R2 than at LEO15, particularly so near-bottom.

The existence of full-depth, albeit disorganized, structures just above $|Ra| = 10^5$ at R2 but not during the prototype event at LEO15 reinforces the conclusion of Gargett and Grosch (2014) that prediction of the type and strength of turbulent structures at intermediate locations in the La-$|Ra|$ plane is highly dependent on water column stability. In the prototype event, the appearance of stratification coincident with $|Ra|$ exceeding 10^5 at the end of the event restricted turbulent motions to an upper layer. Absence of stratification after the September LS event at LEO15 and after the R2 event shown in Figure 13b apparently allows disorganized but still full-depth structures for values of $|\mathrm{Ra}| > 10^5$.

We now demonstrate that weaker C-L vortex forcing may contribute to observed disorganization of full-depth structures at R2. First, it can be shown that at both sites, records with full-depth structures and $Q > 0$ occur at values of $-H/L_{MO}$ that are well below values associated with dominance of unstable convection over stress-driven turbulence in the atmospheric boundary layer (Holtslag and Nieuwstadt, 1986; Gargett and Grosch, 2014). Since $La < 1$ (i.e., C-L forcing dominates stress forcing) for such records, it can be concluded that larger destabilizing buoyancy flux (i.e., larger $Ra \propto Q/g_*^2$ through larger $Q > 0$) is not a primary source of structural disorganization, but rather the smaller values of g_* characteristic of R2 relative to LEO15 documented in Figure 16.

Characteristic LC growth rate g_* is proportional to the geometric mean of two characteristic vertical shears, that of a stress-driven mean current $\partial U/\partial x_3 \sim u_*/H$ and that of a characteristic Stokes shear ($\partial U_S/\partial x_3$). Although u_* during storms is typically larger at R2 than LEO15 (not shown), so is H: observationally, $u_*/H = (6-7) \times 10^{-4}\mathrm{s}^{-1}$ in both locations. Thus the difference in g_* values lies primarily in differences in characteristic

Stokes shear. The observed wavelength/frequency distributions of storm waves, hence depth dependence of U_S, are similar at both sites (not shown). Greater water depth at R2 means that Stokes shear evaluated at a fixed depth fraction is that at deeper actual depth ($x_3 \sim -5$ m for R2 vs. ~ -3 m for LEO15), hence characteristic Stokes shear is smaller for similar wave amplitudes. Despite the fact that waves at R2 (Hs ~2.5 m) are slightly larger than at LEO15 (Hs ~2 m), the depth effect apparently dominates. As seen in Figure 16, maximum values of g_* at R2 are somewhat smaller than those at LEO15, hence the differences between minimum values of $|Ra|$ seen in Figure 15.

Because surface waves at R2 barely reach intermediate character (Fig. 12b), the difference in near-bottom Stokes shear G_* between the two sites is considerably larger than that in g_* (a full factor of 2; see Fig. 14). We suggest that this difference may be of fundamental importance because it affects the total C-L force available to drive full-depth LC in unstratified water columns. Existing theory assumes that LC are driven solely from an upper surface where vertical vorticity produced by a variety of near-surface turbulent processes is available for rotation to horizontal by Stokes shear and amplification by mean shear (Leibovich, 1983). However, C-L vortex forcing will exist wherever there is both a supply of vertical vorticity and nonzero Stokes shear. In a depth-limited system, turbulent vertical vorticity associated with the bottom boundary layer is potentially an additional source of C-L forcing, although one that is critically dependent on the magnitude of Stokes shear near the bottom. It seems plausible that the LC structures at LEO15, where surface waves are of intermediate type and have relatively large near-bottom Stokes shears, are strongly forced from both boundaries, resulting in the highly organized structures observed there. Driving from the bottom is much reduced at R2 because, despite the presence of bottom boundary layer turbulence, the marginal nature of intermediate character achieved by the surface wave field at this deeper site results in much-reduced Stokes shear, hence C-L forcing, near the bottom.

Tejada-Martínez and Grosch (2007) carried out a limited LES investigation of the effects of varying values of λ, the (dominant) surface wave wavelength for fixed H. They found that "for a fixed turbulent Langmuir number La_t, the longer the waves generating LC, the stronger the impact of LC is on the structure of the turbulence in the lower part of the water column." (Note: their $La_t = La^{1/2}$.) La is approximately the same at LEO15 and R2; however, storm-driven surface waves have similar wavelengths while depths differ, so that $\lambda/H \sim 6$ at LEO15, but only ~3 at R2. Our demonstration of lower LC growth rates throughout the water column at R2 (Fig. 16) is consistent with the results of Tejada Martínez and Grosch (2007), suggesting that reduced C-L forcing contributes to the less-organized full-depth structures observed there.

An additional possible contribution to disorganized structures is the instability of paired vortices mentioned in the Introduction. Estimates of L, the horizontal scale of vortex pairs associated with C-L forcing, can be made from observations of apparent period, assuming advection of a fixed crosswind scale by observed crosswind velocity (Gargett and Wells, 2007; Gargett and Grosch, 2014). At both sites, we find $L \simeq \lambda$, that is, the estimated

horizontal scale of the vortex pairs is approximately that of the dominant surface-wave wavelength at the time of the LS event. The lower value of $\lambda/H \simeq L/H \sim 3$ at R2 would thus imply marginal instability of paired vortices under the criterion of Rosenhead (1929).

Finally, tidal velocities are two to three times larger in magnitude at R2 than at LEO15, with degree of structural (dis)organization at R2 observed to vary with tidal phase. Thus an additional or alternate factor weakening structural coherence at R2 may be direct interference by stronger tidal bottom boundary layer turbulence.

The dominant (if any) cause of the less-ordered structures observed at the greater depths of R2 remains to be determined. However, unless the tidal effect proves dominant, coherent LS will not be found in waters much deeper than the 27 m of R2, since the maximum wavelengths of surface waves forced by typical storms, and hence the magnitudes of the first two effects, will be similar across shelves.

7. Summary and conclusions

This work provides detailed descriptions of the mean properties, surface wave fields, and turbulence that accompany a single LS event. Properties of this prototype event have then been compared with those of two additional events, in order to identify conditions common to onset and cessation of LS events.

There are multiple indications that the first essential condition is an unstratified water column. No LS events are observed during the summer season at LEO15, when stratification is maintained by both wind-driven upwelling and strong solar insolation. In the prototype event, which starts with substantial stratification, there is an extensive period of time when LC are confined to a surface layer; this event starts only when stratification disappears from the water column. Event ends are often (though not always) associated with appearance of weak stratification. Although not conclusively causal, since the appearance of stratification caused by mesoscale slumping following relaxation of the wind-driven pressure gradient at the coast coincides with lessening of C-L vortex forcing, strong correlation between stratification and water column backscatter/vertical velocities after the prototype event suggests the importance of even weak stability. The definition of "weak" in this context awaits further investigation. The necessity of an unstratified water column implies that LS events on shallow shelves will occur predominantly when winds favor coastal downwelling. Indeed, fall, winter and late spring, when winds are generally downwelling favorable, are when strong LS events are observed both in 8 months of LEO15 data and in nearly 3 years of subsequent observations at R2.

Langmuir supercells are full-depth velocity structures with strong and highly characteristic phase relationships among components, revealed by vertically overlapping backscatter features associated with familiar surface-origin microbubble clouds in the downwelling zones of LC vortex pairs and less familiar bottom-origin sediment clouds in upwelling zones. Examination of the prototype and two additional events indicates that resuspended

sediment is always available in a thin surface-wave boundary layer when LC reach full depth. Thus the three conditions that must be achieved for onset of LS are those necessary for full-depth LC: 1) an unstratified water column, as discussed above; 2) $La < \sim 0.3$; and 3) $|Ra| < 10^5$, where La and Ra are the nondimensional variables defined by Gargett and Grosch (2014) in discussing cases with destabilizing surface heat fluxes; the present results extend their analysis to stabilizing surface heat fluxes. LS events start when the last of these three conditions is met and end when the first of them is violated. There is no characteristic order in which the three requirements are met or fail.

Onset of a LS event is found to be associated with (although not caused by) the presence of waves of intermediate type. Once waves have transitioned from deepwater to intermediate type, we observe a highly linear relationship between near-surface and near-bottom LC growth rates, explaining why Ra, computed with near-surface parameters, provides an effective measure of the strength of full-depth LC. Using shallow-water wave theory for a single wave, we suggest the form of an explanation for the observed linear relationship; a more complete examination for a broadband wave spectrum is of interest but beyond the scope of this paper.

As waves achieve intermediate type, they are said to "feel bottom": concurrently, the bottom begins to feel the waves. We show that as wave amplitudes increase under storm winds, stress in the thin surface-wave bottom boundary layer rapidly exceeds resuspension thresholds for the full range of particle sizes found in eastern U.S. coast shelf sediments, guaranteeing sediment supply to the upwelling limbs of LC once they reach full depth. The ε_B metric used to estimate onset of surface-wave breaking, hence microbubble supply to the downwelling limbs of LC, was successful in predicting the appearance of surface-origin backscatter features in the prototype (May) and October events but failed in the September event (which may have been more affected by waves remnant from a previous LS event than the other two). It appears that a more complex metric (e.g., Banner et al., 2002), involving the full (possibly directional) wave spectrum may be necessary for the generalized case, but this is, again, beyond the scope of the present paper.

Full-depth velocity structures at the 27-m-deep R2 site off Georgia are only occasionally as well organized as those typical of LS events in 15 m of water at LEO15; in general, the strong phase relationships among near-bottom velocity components are absent, and bottom sediment clouds are less distinct. We suggest three possible reasons for loss of coherence of LS structures at R2 relative to those at LEO15.

1) Decreased forcing: We document that C-L vortex forcing is reduced at R2 throughout the water column, but particularly near bottom, as a result of the marginal nature of intermediate character achieved by the surface-wave field at this deeper site, where $\lambda/H \sim 3$, only half that at LEO15.

2) Instability boundary: If $L/H \sim \lambda/H$, where L is the horizontal scale of the LS and λ the dominant surface wavelength, the difference between λ/H values at the two sites is the difference between stability (LEO15) and marginal instability (R2) of vortex pairs (Rosenhead, 1929).

3) Increased interference: Stronger tidal velocities at R2 may result in interference of tidally generated bottom boundary layer turbulence with the near-bottom structure of LS.

Further work will be necessary to determine the degree to which each proposed mechanism weakens the coherence of LS at R2. If either (or both) of the first two mechanisms is dominant, the question "How deep?" can be answered. Since maximum surface wavelengths generated by typical storms do not vary dramatically over the U.S. East Coast shelves, and LS events are associated with surface waves of intermediate type, it is unlikely that LS structures will be observed in water depths much greater than the 27 m at R2, where waves barely achieve intermediate type. Deeper events could of course occur in storms sufficient to produce surface waves of larger amplitude, wavelength, or both than those ($Hs \sim 3$ m, $L_p \sim 100$ m) typical of nor'easters at R2. If the tidal mechanism dominates, the answer to this question will require detailed analysis of the means by which LS are affected by tidal turbulence.

In the course of detailed examination of the prototype LS event, we also documented two interesting features of LC acting in the surface layer of the stratified water column that existed prior to event onset. First, LC confined to the surface layer were apparently able to generate first-mode internal waves with frequency that of the maximum buoyancy frequency found in the stratified part of the water column. Generation was not continuous, for reasons that may have to do with details of the evolution of either the LC, the underlying density structure, or both.

A second observation was that active LC in the surface layer were ineffective in producing observed mixed-layer deepening, which instead occurred primarily in two separate episodes of Ri lowered by increased mean shear. This observation suggests that LC do not act efficiently as direct agents of deepening but that instead, as a result of quasi-organized structure and enhanced vertical penetration relative to stress-driven turbulence, their primary role is to increase the efficiency of momentum transfer to the surface layer. Enhanced acceleration of a "slab-like" surface layer through the action of LC will contribute to onset of the shear instability that *does* deepen the surface layer, and to the rapidity of wind-driven setup in coastal oceans. The generality of this result is unknown; however, since the nature of LC influence on surface-layer depth is important to appropriate parameterization in both regional coastal models and upper ocean models, it should be the subject of further observational effort at a level commensurate with that reported here.

The effect of LS events on sediment transport is profound. Sediments removed from near-bed beneath upwelling limbs of LS effectively step onto an escalator toward the surface. While the vertical distance achieved depends on particle weight, with only a lighter fraction likely to reach surface, vertical movements of all particles will exceed those produced by "normal" bottom boundary layer turbulence as a result of the quasi-organized nature of LS. Particles thus removed from the low-flow region near the bed enter the strong, vertically homogenized downwind flow associated with LS events (Gargett and Wells, 2007; Tejada-Martínez and Grosch, 2007), providing a powerful mechanism for enhanced sediment transport during these events. An illustration of the extent of potential transport is

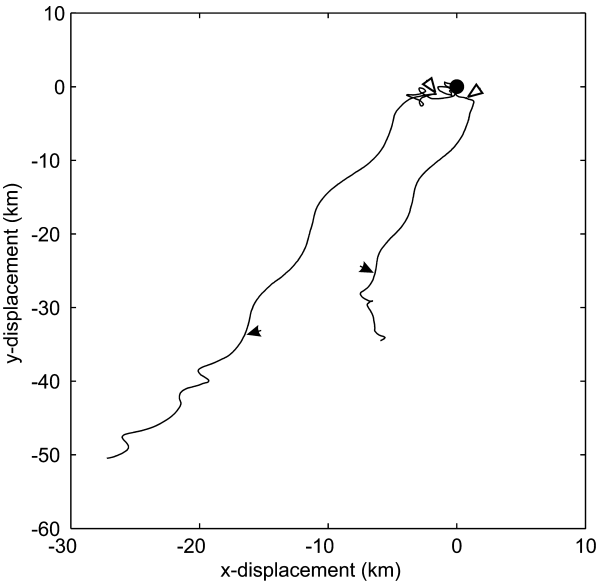

Figure 17. Progressive vector diagrams for two heights above bottom for the prototype event at LEO15. The longer trace is for (mid-bin) height above bottom $h = 8.8$ m, the shorter for $h = 1.2$ m. The black dot is the start of the session; open and filled triangles denote the start of Records 20 through 35.

seen in Figure 17, which shows progressive vector diagrams at two values of height above bottom for the prototype May event. Weather maps for May 17, in the middle of this LS event, show that a strong high-pressure system centered over northern Maine produced winds from the northeast over the entire shelf from Cape Cod to Cape Hatteras; hence the assumption of spatial uniformity necessary for interpretation of the progressive vector diagram as displacements is reasonable. Horizontal distances during the LS event (white to black triangles) are in excess of 40 km at $h = 8.8$ m and $\sim$25 km at $h = 1.2$ m. Evidence that sediment transport is indeed dominated by such events is found in direct measurements of near-bottom sediment transport at a site in Long Bay, South Carolina, over a 4-month period from early February through early May 2004, as reported by Warner et al. (2012). Net transport was dominated by a single event, undoubtedly a LS event forced by a strong nor'easter caused by an offshore low-pressure system. Had measurements included the full water column, dominance of this supercell event would have been even more pronounced.

We also note backscatter evidence of periodic resuspension of sediment in a bottom boundary layer after the prototype event, but not before. This likely results from sediment size class sorting during event cessation, when the heaviest size classes will settle out first, the lightest last. A surface left covered with the finest of silt is more easily remobilized than are the reworked, mixed sediments existing before such an isolated event.

Before concluding, we would like to emphasize (as did Gargett and Grosch, 2014) that it is unclear how much of the present results will apply to LC in deepwater surface mixed layers, primarily because of major differences in the effects of rotation in coastal and deepwater ocean settings. In both coastal data sets discussed here, proximity to a lateral boundary allows establishment of (approximately) shore-parallel mean flow in which rotational forces are primarily balanced by a shore-normal pressure gradient associated with coastal setup. Despite its rotational foundation, once this mean flow has been set up, wind stress on the surface is balanced by bottom stress, a situation formally equivalent to the rotationless wind-forced flow modelled by Tejada Martínez and Grosch (2007). In this case, both models and observations show steady mean flows and turbulent structures, given constant wind forcing. In contrast, absence of lateral boundaries in the deepwater case precludes such a steady state. The mean current resulting from steady wind forcing contains an undamped inertial oscillation, and turbulent properties can be considered only as statistically steady when averaged over several inertial periods (Tejada-Martínez et al., 2009). It seems likely that the type of tools used here, allowing resolution of the three-dimensional fields of both mean and turbulence over extended time periods, would prove fruitful if used in the quite different system of the deepwater surface mixing layer.

Acknowledgments. Research support from the National Science Foundation (OCE0136403 and OCE0927724) and NOAA (NA06RU0139) is gratefully acknowledged. We thank colleagues George Voulgaris and Chester Grosch for help with pesky details. The observations discussed here owe much to the skills of Christopher Powell and Shuang Huang (LEO15), Trent Moore and Julie Amft (R2).

REFERENCES

Banner, M. L., A. V. Babanin, and I. R. Young. 2000. Breaking probability for dominant waves on the sea surface. J. Phys. Oceanogr., *30*, 3145–3160.

Banner, M. L., J. R. Gemmrich, and D. M. Farmer. 2002. Multiscale measurements of ocean wave breaking. J. Phys. Oceanogr., *32*, 3364–3375.

Blanton, B. O., A. Aretxabaleta, F. E. Werner, and H. E. Seim. 2003. Monthly climatology of the continental shelf waters of the South Atlantic Bight. J. Geophys. Res., *108*(C8). doi:10.1029/2002JC001609.

Craik, A. D. D., and S. Leibovich. 1976. A rational model for Langmuir circulations. J. Fluid. Mech., *73*, 401–426.

Csanady, G. T. 1994. Vortex pair model of Langmuir circulation. J. Mar. Res., *52*, 559–581.

Gargett, A. E. and C. E. Grosch. 2014. Turbulence process domination under the combined forcings of wind stress, the Langmuir vortex force, and surface cooling. J. Phys. Oceanogr. *44*, 44–67.

Gargett, A. E., A. E. Tejada-Martínez, and C. E. Grosch. 2008. Measuring turbulent large-eddy structures with an ADCP. I. Vertical velocity variance. J. Mar Res., *66*, 157–189.

——— 2009. Measuring turbulent large-eddy structures with an ADCP. II. Horizontal velocity variance. J. Mar Res., *67*, 569–595.

Gargett, A. E., and J. R. Wells. 2007. Langmuir turbulence in shallow water. I. Observations. J. Fluid Mech., *576*, 27–61.

Gargett, A. E., J. R. Wells, A. E. Tejada-Martinez, and C. E. Grosch. 2004. Langmuir supercells: a mechanism for sediment resuspension and transport in shallow seas. Science, *306*, 1925–1928.

Gnanadesikan, A. 1996. Mixing driven by vertically variable forcing: an application to the case of Langmuir circulation. J. Fluid Mech., *322*, 81–107.

Harcourt, R. R., and E. A. D'Asaro. 2008. Large-eddy simulation of Langmuir turbulence in pure wind seas. J. Phys Oceanogr., *38*, 1542–1562.

Holtslag, A. A. M., and F. T. M. Nieuwstadt. 1986. Scaling the atmospheric boundary layer. Boundary-Layer Met., *36*, 201–209.

Kohut, J. T., S. M. Glenn, and R. J. Chant. 2004. Seasonal current variability on the New Jersey inner shelf. J. Geophys. Res., *109*(C7). doi:10.1029/2003JC001963.

Leibovich, S. 1983. The form and dynamics of Langmuir circulations. Ann. Rev. Fluid Mech., *15*, 391–427.

Madsen, O. S., and W. D. Grant. 1976. Sediment transport in the coastal environment. Rep. 209, Ralph M. Parson Lab., Dep. of Civil Eng., Mass. Inst. of Technol., Cambridge, Mass., 105 pp.

McWilliams, J. C., P. P. Sullivan, and C.-H. Moeng. 1997. Langmuir turbulence in the ocean. J. Fluid Mech., *334*, 1–30.

Münchow, A., and R. J. Chant. 2000. Kinematics of inner shelf motions during the summer stratified season off New Jersey. J. Phys. Oceanog., *30*, 247–268.

Polton, J. A., J. A. Smith, J. A. MacKinnon, and A. E. Tejada-Martínez. 2008. Rapid generation of high-frequency internal waves beneath a wind and wave forced oceanic surface mixed layer. Geophys. Res. Letters, *35*(13). doi:10.1029/2008GL033856.

Rosenhead, L. 1929. The Karman street of vortices in a channel of finite breadth. Phil. Trans. Roy. Soc. London, *228*, 275–330.

Savidge, W. B., A. Gargett, R. A. Jahnke, J. R. Nelson, D. K. Savidge, R. T. Short, and G. Voulgaris. 2008. Forcing and dynamics of seafloor-water column exchange on a broad continental shelf. Oceanography, *21*(4), 179–184.

Sherwood, C.R., J. R. Lacey, and G. Voulgaris. 2006. Shear velocity estimates on the inner shelf off Grays Harbor, Washington, USA. Contl. Shelf Res., *26*, 1995–2018.

Shields, A. 1936. Anwendung der Ähnlichkeitsmechanik auf die Geschiebebewegung: Berlin, Preussische Versuchanstalt für Wasserbau und Schiffbau, Mitteilungen, 26, 25 pp.

Soulsby, R. 1997. Dynamics of Marine Sands: A Manual for Practical Applications. London: Thomas Telford, 249 pp.

Sternberg, R.W. 1968. Friction factors in tidal channels with differing bed roughness. Mar. Geol., *6*, 243–260.

Strang, E. J., and H. J. S. Fernando. 2001. Entrainment and mixing in stratified shear flows. J. Fluid Mech., *428*, 349–386.

Tejada-Martínez, A. E., and C. E. Grosch. 2007. Langmuir turbulence in shallow water. II. Large-eddy simulation. J. Fluid Mech., *576*, 63–108.

Tejada-Martínez, A. E., C. E. Grosch, A. E. Gargett, J. A. Polton, J. A. Smith, and J. A. MacKinnon. 2009. A hybrid spectral/finite difference large-eddy simulator of turbulent processes in the upper ocean. Ocean Modelling, *30*, 115–142.

Thorpe, S. A. 1992. The breakup of Langmuir circulation and the instability of an array of vortices. J. Phys. Oceanogr., *22*, 350–360.

Trowbridge, J. H., and Y. C. Agrawal. 1995. Glimpses of a wave boundary layer. J. Geophys. Res., *100*(C10), 20, 729–743.

Warner, J. C., B. Armstrong, C. S. Sylvester, G. Voulgaris, T. Nelson, W. C. Schwab, J. F. Denny. 2012. Storm-induced inner-continental shelf circulation and sediment transport: Long Bay, South Carolina. Contl. Shelf Res., *42*, 51–63.

Zedel, L., and D. M. Farmer. 1991. Organized structures in subsurface bubble clouds: Langmuir circulation in the open ocean. J. Geophys. Res., *96*, 8889–8900.

Received: *2 February 2014*; revised: *18 August 2014*.